

# Detection of an Earth-sized exoplanet orbiting the nearby ultracool dwarf star SPECULOOS-3

Received: 14 February 2024

Accepted: 10 April 2024

Published online: 15 May 2024

 Check for updates

A list of authors and their affiliations appears at the end of the paper

Located at the bottom of the main sequence, ultracool dwarf stars are widespread in the solar neighbourhood. Nevertheless, their extremely low luminosity has left their planetary population largely unexplored, and only one of them, TRAPPIST-1, has so far been found to host a transiting planetary system. In this context, we present the SPECULOOS project's detection of an Earth-sized planet in a 17 h orbit around an ultracool dwarf of M6.5 spectral type located 16.8 pc away. The planet's high irradiation (16 times that of Earth) combined with the infrared luminosity and Jupiter-like size of its host star make it one of the most promising rocky exoplanet targets for detailed emission spectroscopy characterization with JWST. Indeed, our sensitivity study shows that just ten secondary eclipse observations with the Mid-InfraRed Instrument/Low-Resolution Spectrometer on board JWST should provide strong constraints on its atmospheric composition and/or surface mineralogy.

At the end of the main sequence, ultracool dwarf stars (UDS)<sup>1</sup> have spectral types between M6.5 and L2, masses between 0.07 and 0.1 solar masses ( $M_{\odot}$ ), sizes similar to Jupiter and effective temperatures between 2,200 and 2,850 K (ref. 2). The Search for Planets Eclipsing Ultra-cool Stars (SPECULOOS) project<sup>3–5</sup> aims to perform a volume-limited (40 pc) transit search of ~1,650 very-low-mass stars and brown dwarfs, including ~900 UDS<sup>6</sup>. It is based on a network of six robotic 1-m-aperture telescopes: the four telescopes of the SPECULOOS-South Observatory (SSO) in Chile<sup>7</sup>, Artemis, the first telescope of the SPECULOOS-North Observatory (SNO) in Tenerife<sup>8</sup>, and the SAINT-EX telescope in San Pedro Mártir Observatory in Mexico<sup>9</sup>. SPECULOOS achieved its first main result in 2015 with the discovery, by its prototype on the robotic 60 cm telescope Transiting Planets and Planetesimals Small Telescope (TRAPPIST)<sup>10</sup>, of a system composed of seven Earth-sized planets in close orbits around an M8-type UDS at 12 pc (refs. 11,12). More recently, SPECULOOS discovered a super-Earth orbiting in the habitable zone of LP 890-9 (also known as SPECULOOS-2, TOI-4306), an M6-type dwarf star at 32 pc (ref. 13).

SPECULOOS-3 (aka LSPM J2049+3336) is an isolated UDS of spectral type M6.5 ± 0.5 located 16.75 pc away. It is one of the ~365

SPECULOOS Program 1 targets that are small and close enough to make the detailed atmospheric characterization of a temperate Earth-sized planet possible with JWST<sup>6</sup>. It was observed by SAINT-EX for five nights in 2021, and by SNO-Artemis for three nights in 2022. Visual inspection of the 2021 and 2022 light curves showed some transit-like structures that motivated future intensive monitoring of the star. It was thus re-observed by SNO-Artemis from July to September 2023. In total, 18 transit-like structures were observed by SNO-Artemis in 2023 and could be related to a period of ~0.72 d. Furthermore, the other transit-like structures in the 2021 (SAINT-EX) and 2022 (SNO-Artemis) light curves corresponded to the identified transit ephemeris (Fig. 1). Follow-up photometric observations were also made to confirm the transit and its achromatic nature using the SSO 1 m telescopes, the TRAPPIST-North 0.6 m telescope at Oukaïmeden Observatory in Morocco, the 1.5 m telescope at Sierra Nevada Observatory in Spain, the Multicolor Simultaneous Camera for studying Atmospheres of Transiting exoplanets 3 (MuSCAT3) instrument on the 2 m Faulkes North telescope in Hawaii, the 3.8 m UK Infrared Telescope (UKIRT) in Hawaii and the High Performance Camera (HiPERCAM) instrument on the 10 m Gran Telescopio Canarias (GTC) telescope at La Palma (Fig. 2).

✉ e-mail: [michael.gillon@uliege.be](mailto:michael.gillon@uliege.be)

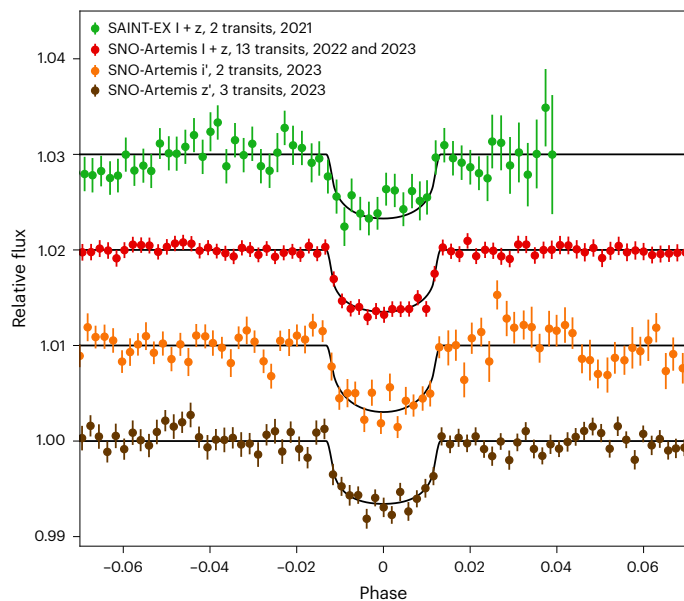


**Fig. 1 | Discovery transit photometry of SPECULOOS-3 b.** Transit photometry obtained by SAINT-EX and SNO-Artemis between 2021 and 2023 (phase-folded, detrended and binned with a 2 min bin width). The light curves are shifted along the y axis for clarity. The SAINT-EX and SNO measurements in the I + z, i' and z' filters are, on average, the means of 2.8, 21.6, 6.0 and 2.5 photometric data points. The error bars are the mean errors of the points within the bin divided by the square root of the number of points. The black lines show the best-fit transit models.

New spectroscopic observations with the Kast Double Spectrograph mounted on the 3 m Shane telescope at Lick Observatory (Fig. 3a), the SpeX spectrograph mounted on the 3 m NASA InfraRed Telescope Facility (IRTF) telescope in Hawaii (Fig. 3b) and the Calar Alto high-Resolution search for M dwarfs with Exoearths with Near-infrared and optical Échelle Spectrograph (CARMENES) mounted on the 3.5 m telescope at Calar Alto Observatory, as well as high-resolution images obtained with the 'Alopeke instrument on the Gemini North telescope in Hawaii, were gathered. Combined with archival absolute magnitudes and the Gaia Extended Data Release 3 (EDR3) parallax, some of the new spectra (following flux calibration) enabled the luminosity of the star to be measured as  $0.000835 \pm 0.000019 L_{\odot}$  (where  $L_{\odot}$  is the luminosity of the Sun) following the procedure described in ref. 14 and references therein.

## Results

Two astrophysical cases had to be excluded to confirm the planetary nature of the candidate. The first case is that of a background eclipsing binary blended with the target's images in the data. Owing to the high proper motion of the target ( $0.46 \text{ arcsec yr}^{-1}$ ), archival images directly refuted this hypothesis by confirming that no background source of significant brightness is located behind its current position (Extended Data Fig. 1). The second case is that of a bound eclipsing binary companion. Several factors argue against this hypothesis when considered individually, and allow us to fully discard it when considered globally: (1) the stability of the star's radial velocity at the  $50 \text{ m s}^{-1}$  level over a 1 yr period as inferred from APOGEE spectra<sup>15</sup>, and the lack of a radial velocity slope larger than  $5 \text{ m s}^{-1} \text{ d}^{-1}$  over the two month period covered by observations of the CARMENES high-resolution spectrograph; (2) the non-detection of a companion object in the GEMINI North high-resolution images (Extended Data Fig. 2); (3) the non-detection of a secondary spectrum in the CARMENES, Kast and SpeX spectra (Fig. 3); (4) the fact that the global spectral energy distribution of the target is closely fitted by the spectral model of an isolated -M6.5 dwarf (Extended Data Fig. 3); (5) the excellent agreement between the stellar density inferred from the transits ( $55.1^{+2.0}_{-3.7} \rho_{\odot}$ , where  $\rho_{\odot}$  is the density

of the Sun) and that deduced from the basic parameters of the star ( $55 \pm 15 \rho_{\odot}$ ); and (6) the achromatic nature of the transit depth from  $\sim 470 \text{ nm}$  (g' filter) to  $\sim 2.2 \mu\text{m}$  (Fig. 2).

The age of the system is constrained to  $6.6^{+1.8}_{-2.4} \text{ Gyr}$  from its kinematics (Methods), and the star's luminosity, mass and radius are  $0.084 \pm 0.002\%$ ,  $10.1 \pm 0.2\%$  and  $12.3 \pm 0.2\%$  of those of the Sun, respectively. Just slightly larger than TRAPPIST-1, SPECULOOS-3 is the second-smallest main sequence star found to host a transiting planet (Fig. 4a). The small size of the host star—only slightly larger than Jupiter—translates to an Earth-like radius for the transiting planet, as deduced from its  $\sim 0.5\%$  transit depth. Table 1 presents the physical properties of the system, as derived from a global Bayesian analysis of the transit photometry (including a priori knowledge of its stellar properties) with an adaptive Markov chain Monte Carlo (MCMC) code (Methods).

The planet is very similar in size to the Earth:  $0.977 \pm 0.022 R_{\oplus}$ . Its equilibrium temperature is  $553 \pm 8 \text{ K}$ , assuming a null Bond albedo and a full heat redistribution. Its mass, and thus its composition, remains unconstrained by our observations thus far. Nevertheless, several factors strongly suggest a rocky composition. From a theoretical point of view, the intense extreme ultraviolet ( $1\text{--}1,000 \text{ \AA}$ ) emission of low-mass stars during their early lives<sup>16</sup> makes it unlikely that such a small planet on such a short orbit could have maintained a substantial envelope of hydrogen<sup>17,18</sup>. From an empirical point of view, SPECULOOS-3 b falls well within the rocky side of the radius gap—that is, the paucity of planets with radii between 1.5 and  $2 R_{\oplus}$  attributed to photo-evaporative processes<sup>19–23</sup>. We also note that all of the known Earth-sized planets in the NASA exoplanet archive<sup>24</sup> have masses that imply rocky compositions.

Ultimately, measuring the mass of SPECULOOS-3 b is essential to determine whether it is indeed rocky, and to further constrain its composition. By our estimates, a reasonable observing programme ( $<5$  nights) that would be able to detect the radial velocity signal of the planet's Doppler reflex motion could be accomplished using state-of-the-art spectrographs (Methods). Such observations should be able to differentiate between Earth-like, iron-poor and water-rich compositions<sup>22</sup>.

## Discussion

TRAPPIST-1 b is the closest analogue to SPECULOOS-3 b in terms of host star size ( $0.123 R_{\odot}$  versus  $0.119 R_{\odot}$ ), planet size ( $0.98 R_{\oplus}$  versus  $1.12 R_{\oplus}$ ) and equilibrium temperature ( $553 \text{ K}$  versus  $400 \text{ K}$ ) (Fig. 4). Nevertheless, the two systems seem to be very different: TRAPPIST-1 hosts a resonant system of seven short-orbit rocky planets, while an intensive photometric monitoring campaign of SPECULOOS-3 with SNO and MuSCAT3 failed to detect any outer transiting planets over a 10 day period range (Methods). This indicates that both systems had different formation/evolution histories. As outlined by recent works, resonant systems like TRAPPIST-1 are rare because they are prone to disruption by dynamical instabilities<sup>25–27</sup>. SPECULOOS-3 b could thus be the outcome of such a disruption. Outer planets may still exist, but on much longer and/or mutually inclined orbits. Nevertheless, we cannot exclude the possibility that outer well-aligned planets do exist, but that they are just too small to be detected with current observations (Methods).

With current irradiation 16 times larger than Earth's, which should have been much larger during the  $\sim 800 \text{ Myr}$  pre-main sequence phase of the star, the possibility of it retaining a substantial secondary atmosphere is slim. Nevertheless, it is possible that a volatile-rich initial composition could have sustained a steady-state secondary atmosphere despite this adverse environment<sup>28–30</sup>. Compared with the more temperate TRAPPIST-1 planets, SPECULOOS-3 b has the advantage that transit transmission spectroscopy<sup>31</sup> or emission or phase curve photometry<sup>32,33</sup> are not the only methods available to assess the presence of an atmosphere. Indeed, the planet is hot enough and its host star small and infrared-bright enough to make it possible to measure its dayside emission spectrum with the MIRI/LRS instrument aboard JWST. Figure 4b shows how SPECULOOS-3 b compares in terms of its

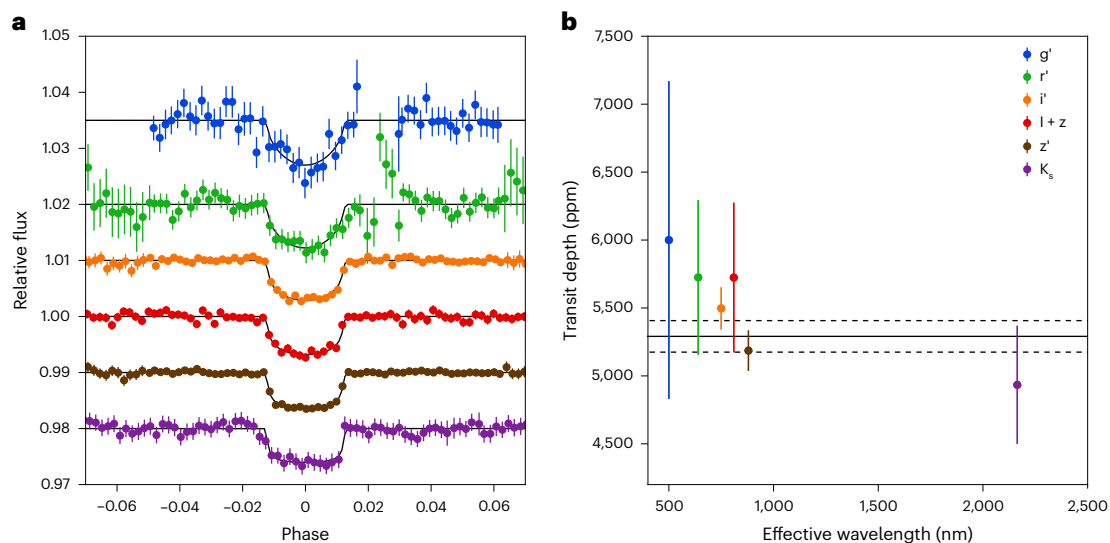


**Fig. 2 | Optical and infrared transit photometry of SPECULOOS-3 b.** **a**, Phase-folded transit photometry of SPECULOOS-3 b in the  $g'$ ,  $r'$ ,  $i'$ ,  $I+z$ ,  $z'$  and  $K_s$  filters (from top to bottom). The photometry are binned with a 2 min bin width and the light curves are shifted along the  $y$  axis for clarity. The  $g'$ ,  $r'$ ,  $i'$  and  $z'$  light curves are dominated by the extremely precise GTC/HiPERCAM light curves from only one transit, while the  $K_s$  light curve is the stack of two transits observed by UKIRT/WFCAM in the  $K_s$  filter. The  $g'$ ,  $r'$ ,  $i'$ ,  $I+z$ ,  $z'$  and  $K_s$  measurements are, on average, the means of 7.6, 5.3, 17.4, 16.2, 26.9 and 17.7 photometric data points. The error bars are the mean errors of the points within the bin divided by the

square root of the number of points. The black lines show the best-fit transit models. **b**, Measured transit depths in the different filters (dots with error bars). The measurements and the errors are, respectively, the means and the standard deviations of the posterior probability distributions derived from the global MCMC analysis. The measurements are compared with the transit depth measured in the global MCMC analysis assuming a common transit depth (dashed lines mark  $1\sigma$  error bars). All measurements agree at better than  $1\sigma$  with the common transit depth measurement.

potential as a target for emission spectroscopy with other known transiting terrestrial planets ( $R_p < 1.6 R_\oplus$ ) that are cool enough ( $T_{\text{eq}} < 880$  K) to have a dayside made of solid rock. Planets with  $T_{\text{eq}} > 880$  K are expected to have molten (lava) surfaces and no atmospheres, except perhaps for vaporized rocks<sup>34</sup>. The potential for investigating these planets with emission spectroscopy is quantified using the ESM<sup>35</sup>, which is proportional to the expected signal-to-noise ratio of a JWST secondary eclipse detection at mid-IR wavelengths. With an ESM value of 7.8, SPECULOOS-3 b is one of the smallest planets above the recommended threshold of ESM = 7.5 (ref. 35) that identifies the top targets for emission spectroscopy with JWST.

Such observations could not only reveal the presence of an atmosphere while avoiding the critical problem of stellar contamination inherent to transit transmission spectroscopy<sup>36</sup> (as observed for TRAPPIST-1 b (ref. 31) or GJ 1132 b (ref. 37); see details in Methods), but also constrain the mineralogical surface of this Earth-sized exoplanet, if airless. We explored the possibility of revealing the nature of the planet with the JWST in emission. We simulated emission spectroscopy observations with the JWST MIRI/LRS mode using PandExo (Methods). We then modelled the emission spectra of several plausible atmospheric scenarios and bare rock surfaces (Methods). These models included CO<sub>2</sub>-dominated or H<sub>2</sub>O-dominated atmospheres, as well as surfaces resulting from various geological configurations: primary crusts from the solidification of a magma ocean (ultramafic and feldspathic), secondary crusts produced by volcanic eruptions (basaltic) or tertiary crusts produced by plate tectonics (granitoid). We found that with only ten occultations observed with MIRI/LRS we could reach the required precision to assess the presence of an atmosphere and distinguish between the most plausible atmospheric scenarios, or, if the planet is airless, distinguish between 50% of competing surface models at  $4\sigma$  (Fig. 5 and Extended Data Tables 1 and 2). Finally, if the planet is airless, emission spectroscopy can also be used to reveal the planet's geological history by constraining the surface emissivity spectrum and indirectly its albedo. Indeed, old bare-rock planets are expected to be much darker than those with fresh geologic surfaces

due to the effect of space weathering (as observed on Mercury or the Moon<sup>38</sup>). Space weathering timescales are short ( $\approx 100$  yr) for close-in planets around active stars like SPECULOOS-3 b, such that any detection of a high-albedo dayside would require the planet's surface to be geologically very young and indicate the presence of active volcanism or tectonic overturn (Extended Data Fig. 4).

These results motivate a dedicated study of SPECULOOS-3 b through emission spectroscopy with JWST, and encourage us to pursue the search for, and detailed study of, the still poorly understood terrestrial planets in orbit around ubiquitous UDS.

## Methods

### Discovery SPECULOOS photometry

The first SPECULOOS observations of the target were acquired in 2019 and 2021 with the SAINT-EX 1 m telescope<sup>9</sup> in the  $I+z$  filter. Two of the 2021 light curves included a transit of SPECULOOS-3 b. They were noticed, but the star was not ranked then as a high-priority target because of the high level of correlated noise in these two light curves due to bad weather conditions. In July 2022, the SNO-Artemis 1 m telescope<sup>8</sup> observed the target for three nights, also in the  $I+z$  filter. One of the three resulting light curves (29 July 2022) showed a clear transit-like signature. Intensive monitoring of the star was then initiated from July 2023, first with SNO-Artemis. Several clear transit-like structures showed up in subsequent light curves. They could be related to a period of  $-0.719$  d, and their shape (duration, depth) was consistent with an Earth-sized planet transiting the star (Fig. 1). SNO-Artemis pursued its monitoring of the star up to the end of September 2023, resulting in 37 light curves of 2 h or more in duration. Several transit windows were also observed in August and September 2023, with some of or all the four 1 m telescopes of the SSO<sup>7</sup> at ESO Cerro Paranal Observatory in Chile. Some of these observations were taken in the  $I+z$  filter, others in the  $i'$  and  $z'$  filters to assess the chromaticity of the transit. In total, SNO-Artemis observed 18 transits of SPECULOOS-3 b, and SSO telescopes observed five of them (Supplementary Table 1).

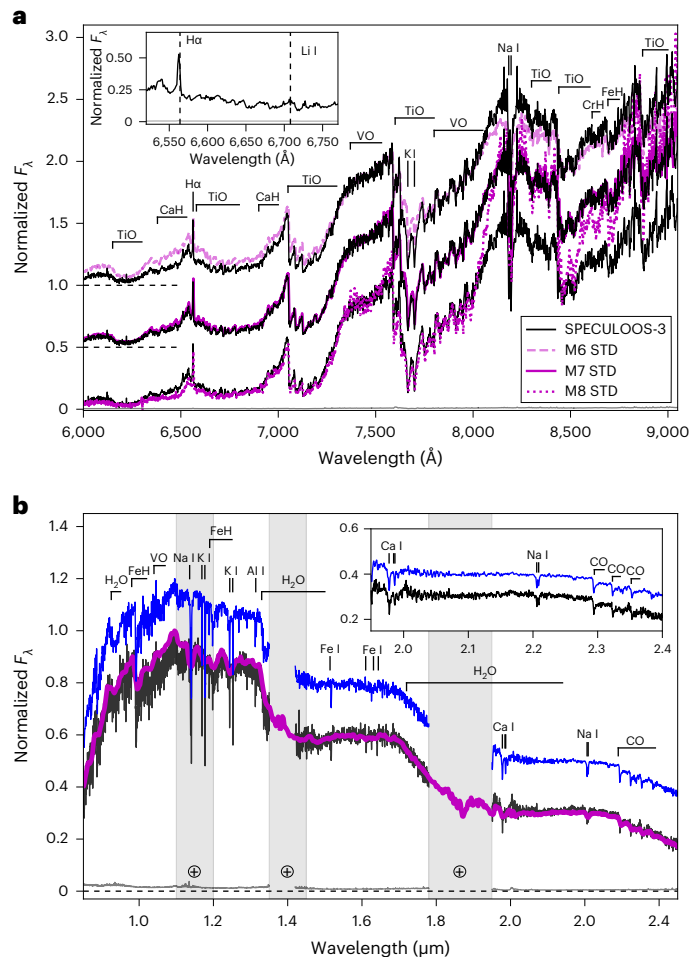


**Fig. 3 | Optical and infrared spectroscopy of SPECULOOS-3.** **a**, Normalized Kast red-optical spectrum of SPECULOOS-3 compared with M6, M7 and M8 spectral standards (STD) from ref. 53 with an M7 spectral type providing the best fit (Methods).  $F_{\lambda}$  flux. Individual comparisons are offset vertically in steps of 0.5, and the spectral flux uncertainties are indicated by the grey line along the bottom. Prominent line and molecular features in the optical spectra of late-M dwarfs are labelled, and the inset shows a close-up of the region encompassing H $\alpha$  6,563 Å emission (detected) and Li I 6,708 Å absorption (not detected). **b**, Normalized SpeX near-infrared spectrum of SPECULOOS-3 (short-wavelength cross-dispersed data in black and prism data in magenta) compared with a medium-resolution spectrum of the M6 dwarf Wolf 359 (blue line, offset by 0.2 flux units). Prominent spectral features of M dwarfs are noted, and regions of high telluric absorption ( $\oplus$ ) are shaded grey. The grey line at the bottom of the plot illustrates the uncertainties for the target spectrum. The inset box highlights the K-band region and its metallicity-sensitive Ca I, Na I and CO features, which are nearly identical between SPECULOOS-3 and Wolf 359.

### Host star properties

SPECULOOS-3 (also known as 2MASS J20492745+3336512 and LSPM J2049+3336) was identified as a high-proper-motion stellar object in 2005<sup>39</sup>, and as a nearby late-type M dwarf in 2014<sup>40</sup>. Spectra taken by the SDSS-3 APOGEE survey led to the first effective temperature estimate of 2,765–2,800 K and an upper limit of 8 km s<sup>-1</sup> for its  $v \sin i_*$  (ref. 41), with  $i_*$  the stellar inclination angle. The three barycentric radial velocities measured from APOGEE spectra (two in 2013, one in 2014) were stable at the 50 m s<sup>-1</sup> level, supporting the hypothesis of an isolated star<sup>42</sup>. On the basis of photometric data and the star's Gaia DR2 parallax (59.733 ± 0.088 mas; ref. 43<sup>44</sup>), a spectral type of M6.5 ± 1.5 was estimated.

We observed SPECULOOS-3 twice with the SpeX near-infrared spectrograph<sup>45</sup> on the 3.2 m NASA IRTF. On 30 August 2021 (UT),

we collected a medium-resolution spectrum ( $\lambda/\Delta\lambda \approx 2,000$ ) using the short-wavelength cross-dispersed mode, covering 0.80–2.42 μm. On 11 August 2023 (UT), we collected a low-resolution spectrum ( $\lambda/\Delta\lambda \approx 120$ ) using the prism-dispersed mode, covering 0.70–2.52 μm. All data were reduced using Spextool v4.1<sup>46</sup>. The final spectra are shown in Fig. 3b. The short-wavelength cross-dispersed and prism-dispersed spectra have median signal-to-noise ratios of 55 and 250 per pixel, respectively. To assign an infrared spectral type, we used the SpeX Prism Library Analysis Toolkit SPLAT<sup>47</sup> to compare the short-wavelength cross-dispersed spectrum to spectral standards in the IRTF Spectral Library<sup>48,49</sup>, finding a best match to the M6 dwarf Wolf 359 (Fig. 3b). We also compared the prism data with low-resolution standards defined in ref. 50, and found a best match in the 0.8–1.3 μm range to the M7 standard VB 8. We therefore adopted an infrared spectral type of M6.5 ± 0.5 for SPECULOOS-3. Using the relation of ref. 51 and following the approach of ref. 13, we estimated an iron abundance of [Fe/H] = +0.08 ± 0.11.

We obtained a red optical spectrum of SPECULOOS-3 with the Kast Double Spectrograph<sup>52</sup> on the 3 m Shane Telescope at Lick Observatory on 29 September 2022 (UT). We used the red channel with 600/7,500 grating and 1.5"-wide slide to obtain 6,000–9,500 Å spectra at an average resolution of  $\lambda/\Delta\lambda = 1,900$ . Data were reduced using the kastredux package available at <https://github.com/aburgasser/kastredux>. The final spectrum (Fig. 3a) has a signal-to-noise ratio of 90 at 8,350 Å. We determined an optical classification by comparing it to late-M dwarf spectral templates from ref. 53, and found the M7 standard provided the best fit. Index-based classifications<sup>54–56</sup> indicated a classification closer to M6. We therefore adopted a mean optical classification of M6.5 ± 0.5, consistent with our infrared data. We measured the metallicity statistic  $\zeta = 1.026 \pm 0.005$  (ref. 57), consistent with [Fe/H] = +0.04 ± 0.20 using the calibration of ref. 58, also consistent with our infrared data.

We performed an analysis of the broadband spectral energy distribution (SED) of the star together with the Gaia DR3 parallax with no systematic offset applied (see, for example, ref. 59) to determine an empirical measurement of the stellar radius, following the procedures described in refs. 14, 60, 61. We pulled the JHK<sub>s</sub> magnitudes from 2MASS, the W1–W3 magnitudes from WISE, the G<sub>BP</sub> and G<sub>RP</sub> magnitudes from Gaia, and the gzy magnitudes from Pan-STARRS. Together, the available photometry spans the full stellar SED over the wavelength range 0.4–10 μm (Extended Data Fig. 3). We also used the absolute flux-calibrated Kast and SpeX spectrophotometry for comparison (see above). We fitted the SED using PHOENIX stellar atmosphere models<sup>62</sup>, with the free parameters being  $T_{\text{eff}}$  and metallicity ([Fe/H]), taking the V-band extinction coefficient  $A_V = 0$  due to the proximity of the system to Earth. The resulting fit (Extended Data Fig. 3) has a best-fit  $T_{\text{eff}} = 2,680 \pm 60$  K and [Fe/H] = -0.15 ± 0.25, with a reduced  $\chi^2$  of 2.1. Both values were consistent with the adopted values inferred as described in the next section. Integrating the model SED gave the bolometric flux at Earth,  $F_{\text{bol}} = 9.54 \pm 0.22 \times 10^{-11}$  erg s<sup>-1</sup> cm<sup>-2</sup>. Taking this  $F_{\text{bol}}$  and the Gaia parallax directly provided the bolometric luminosity,  $L_{\text{bol}} = 8.35 \pm 0.19 \times 10^{-4} L_{\odot}$ , which with the Stefan–Boltzmann relation implied a stellar radius  $R_* = 0.1342 \pm 0.0062 R_{\odot}$ . We note that this radius, together with the spectroscopically-derived  $v \sin i$  upper limit from APOGEE (8 km s<sup>-1</sup>) implied a projected rotation period of  $P_{\text{rot}}/\sin i > 0.85$  d.

We adopted the weighted average of the Kast (visible) and SpeX (near-IR) measurements for the star's metallicity: [Fe/H] = 0.07 ± 0.10. Using the Gaia EDR3 parallax and the 2MASS H magnitude of the star, we estimated the effective temperature of SPECULOOS-3 to be  $T_{\text{eff}} = 2,829 \pm 30$  K using the empirical relationship  $T_{\text{eff}}(M_H)$  of ref. 63, and accounting for its internal error of 29 K. This  $T_{\text{eff}}$  value is in excellent agreement with those inferred by ref. 41 and ref. 15, but in tension with that inferred from our SED fitting (2,680 ± 60 K). In this context, we decided to adopt (as before in our global analysis, see below) the weighted average of the two estimates and an error bar large enough

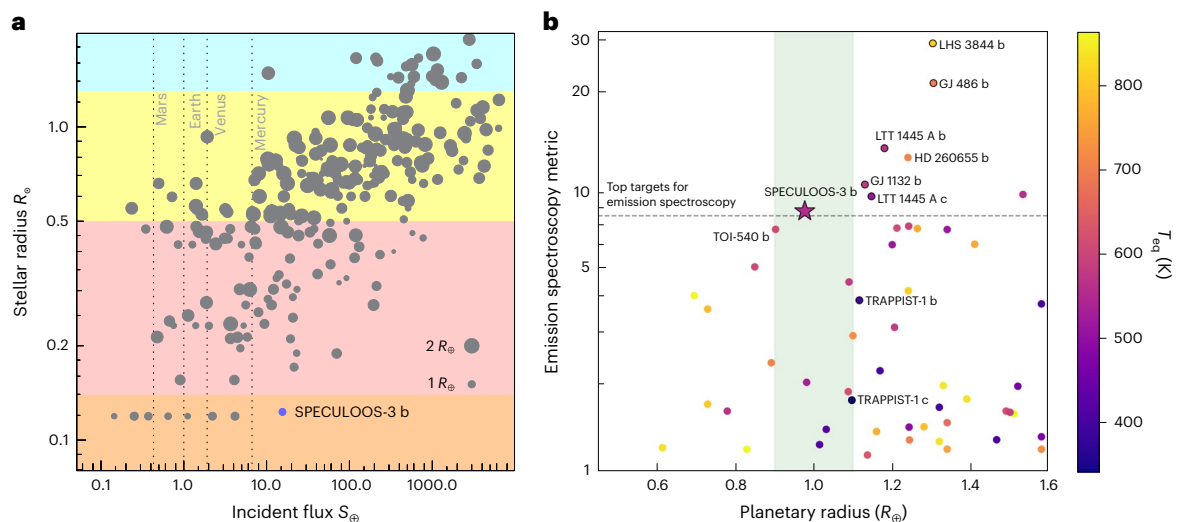


**Fig. 4 | Comparison of SPECULOOS-3 b with other rocky exoplanets.**

**a**, Sizes of host stars in solar radii ( $R_{\odot}$ ) and incident stellar fluxes of known sub-Neptune-sized exoplanets. The sizes of the symbols scale linearly with the radius of the planets. The background is colour-coded according to stellar size (in solar masses), with the UCD regime shown in orange. The red, yellow, and blue shadings show, respectively, the regimes of M-dwarfs, of G-dwarfs and K-dwarfs, and of more massive stars. The positions of the terrestrial Solar System planets are shown for reference. One can see that SPECULOOS-3 b extends the unique planet sample of TRAPPIST-1 to a larger stellar flux. **b**, SPECULOOS-3 b in the context of other known transiting terrestrial exoplanets (with a planetary

radius  $R_p < 1.6$  Earth radii ( $R_{\oplus}$ )) that are cool enough (equilibrium temperature  $T_{\text{eq}} < 880$  K; ref. 34) to have a dayside made of solid rock (in contrast to hotter magma worlds with molten surfaces). The planets are shown as a function of their radius and emission spectroscopy metric (ESM)<sup>35</sup>. Data points are colour-coded according to their  $T_{\text{eq}}$ . The shaded green area highlights planetary radii most similar to Earth's (0.9–1.1  $R_{\oplus}$ ). The dashed horizontal line represents the ESM threshold of 7.5 recommended by ref. 35 to identify the top targets for emission spectroscopy with JWST. SPECULOOS-3 b is one of the smallest planets amenable to emission spectroscopy with MIRI/LRS. Data from ref. 116.

to encompass the value of 2,680 K from the SED fitting, resulting in  $T_{\text{eff}} = 2,800 \pm 120$  K. We then used the Stefan–Boltzmann law to compute the stellar radius as  $R_{\star} = 0.123 \pm 0.011 R_{\odot}$  from our adopted  $T_{\text{eff}}$  and measured  $L_{\text{bol}}$ . Finally, we estimated the mass of the star to be  $M_{\star} = 0.1017 \pm 0.0024 M_{\odot}$  from its 2MASS K magnitude and its Gaia EDR3 parallax, using the relationship of ref. 64 and accounting for its internal error of 0.0023  $M_{\odot}$ .

Using the PyAstronomy/ga\_l\_uvw routine<sup>65</sup> based on the algorithm of ref. 66, with the Gaia EDR3 coordinates and proper motions of the star<sup>67</sup> and its APOGEE radial velocity<sup>15</sup> as input, we computed the following galactic velocities in the local standard of rest frame for SPECULOOS-3:  $U = 47.16 \pm 0.29$  km s<sup>-1</sup>,  $V = 21.34 \pm 0.43$  km s<sup>-1</sup>, and  $W = -3.68 \pm 0.26$  km s<sup>-1</sup>. These values were computed using the local standard of rest frame correction of ref. 68,  $U, V, W_{\odot} = [+8.50, +13.38, +6.49]$ . These velocities would place the star, statistically speaking, in the thin disk of our Galaxy, suggesting an age of less than 8 Gyr (ref. 69). A more careful analysis comparing the kinematics of SPECULOOS-3 to nearby co-moving stars (within 5 km s<sup>-1</sup> in  $UVW$ ) with a similar metallicity (within 0.2 dex) using data from GALAH DR3<sup>70</sup> yielded an uncertainty-weighted average age of  $6.6_{-2.4}^{+1.8}$  Gyr.

We also ran stellar evolution modelling using structure models presented in ref. 71. We used the luminosity and metallicity as derived above as constraints. We obtained a stellar mass ( $M_{\star} = 0.1001 \pm 0.0015 M_{\odot}$ ), radius ( $R_{\star} = 0.125 \pm 0.002 R_{\odot}$ ) and effective temperature ( $T_{\text{eff}} = 2,780 \pm 30$  K) in excellent agreement with the estimates obtained above. Finally, the pre-main sequence phase for a 0.10  $M_{\odot}$  star lasts about 800 Myr, suggesting a greater age for SPECULOOS-3.

### TESS photometry

We downloaded the TESS 2-min-cadence PDCSAP Sector 41 and 55 light curve using lightkurve<sup>72</sup>. Analysis of the TESS photometry of SPECULOOS-3 revealed its flaring nature, led to a marginal detection of the transit of SPECULOOS-3 b and did not result in an unambiguous determination of its rotation period (Supplementary Fig. 1).

### MuSCAT2 photometry

A transit of SPECULOOS-3 b was observed on 12 August 2023 with the MuSCAT2 multi-imager instrument<sup>73</sup> at the Telescopio Carlos Sánchez located at the Teide Observatory (Spain). Unfortunately, the night was cloudy and the resulting photometry was too noisy to be of any scientific use.

### MuSCAT3 photometry

We used the 2.0 m Faulkes Telescope North at Haleakala Observatory located in Hawaii to observe SPECULOOS-3. The telescope is equipped with the MuSCAT3 multi-band imager<sup>74</sup>. The campaign was started on the single night of 3 September 2023, and then from 15 September 2023 to 26 September 2023. The main goal of this campaign was to search for additional transiting planets in the system. During this campaign, we observed two full transits of SPECULOOS-3 b on UT 17 and 19 September 2023 in the Sloan  $g', r', i'$  and  $z_s$  filters. All datasets were calibrated using the standard LCOGT BANZAI pipeline<sup>75</sup>, and photometric measurements were extracted in an uncontaminated target aperture using the PROSE pipeline<sup>76</sup>.

### TRAPPIST-North photometry

TRAPPIST-North is a 60 cm robotic telescope located at Oukaïmeden Observatory in Morocco<sup>77–79</sup>. It observed a total of six transits of SPECULOOS-3 b on 2, 4, 5, 17, 28 and 30 August 2023 in the I + z and Sloan-z' filters. When combined, the resulting light curves confirmed the transit, but we did not include them in our global analysis as their precision was substantially lower than the precision obtained with the other telescopes.

### T150 photometry

We conducted a full-transit observation of SPECULOOS-3 b on 20 September 2023 using the T150 at the Sierra Nevada Observatory in Granada (Spain). The T150 is a 150 cm Ritchey–Chrétien telescope equipped with a thermoelectrically cooled 2 K × 2 K Andor iKon-L BEX2DD CCD camera with a field of view of 7.9' × 7.9' and pixel scale of 0.232". We used the

**Table 1 | Parameters of the SPECULOOS-3 system**

Parameter	Value $\pm 1\sigma$ error
Stellar parameters	
Spectral type	M6.5 $\pm 0.5$
Parallax	59.701 $\pm 0.043$ mas
Distance	16.750 $\pm 0.012$ parsec
Right ascension (RA) (J2000)	20h 49min 27.440s
Declination (dec) (J2000)	+33° 36' 50.96"
Proper motion (RA)	-207.809 $\pm 0.038$ mas yr <sup>-1</sup>
Proper motion (dec)	-412.815 $\pm 0.037$ mas yr <sup>-1</sup>
Radial velocity	17.816 $\pm 0.019$ km s <sup>-1</sup>
U galactic velocity	47.16 $\pm 0.29$ km s <sup>-1</sup>
V galactic velocity	21.34 $\pm 0.43$ km s <sup>-1</sup>
W galactic velocity	-3.68 $\pm 0.26$ km s <sup>-1</sup>
G magnitude	15.380 $\pm 0.003$ mag
K magnitude	10.541 $\pm 0.016$ mag
Mass	0.1009 $\pm 0.0024$ M <sub>⊙</sub>
[Fe/H]	+0.07 $\pm 0.10$ dex
Luminosity	0.000835 $\pm 0.000019$ L <sub>⊙</sub>
Effective temperature (T <sub>eff</sub> )	2800 $\pm 29$ K
Radius	0.1230 $\pm 0.0022$ R <sub>⊙</sub>
Density	54.7 $\pm 2.5$ ρ <sub>⊙</sub>
log <sub>10</sub> [surface gravity (cgs)]	5.265 $\pm 0.014$ dex
Projected rotational velocity vsini	4.2 $\pm 0.4$ km s <sup>-1</sup>
Age	6.6 <sup>+1.8</sup> <sub>-2.4</sub> Gyr
Planetary parameters	
Orbital period	0.71912603 $\pm 0.00000057$ d
Mid-transit time	BJD <sub>TDB</sub> 2459790.58344 $\pm 0.00032$
Transit depth (R <sub>p</sub> /R <sub>★</sub> ) <sup>2</sup>	5,291 $\pm 116$ ppm
Transit impact parameter	0.124 $\pm 0.085$ R <sub>★</sub>
Transit duration	27.36 $\pm 0.23$ min
Orbital inclination	89.44 $\pm 0.39$ deg
Orbital semi-major axis	0.007330 $\pm 0.000055$ AU
	12.81 $\pm 0.20$ R <sub>★</sub>
T <sub>eq</sub> (assuming A <sub>b</sub> =0 and full heat redistribution.)	553 $\pm 8$ K
Irradiation	15.54 $\pm 0.42$ S <sub>⊙</sub>
Radius	0.977 $\pm 0.022$ R <sub>⊕</sub>
	0.07273 $\pm 0.00080$ R <sub>★</sub>

The properties of the SPECULOOS-3 system were gathered from different sources or derived through a global Bayesian analysis of the transit photometry (Methods). BJD<sub>TDB</sub>, barycentric Julian date expressed in barycentric dynamical time; R<sub>★</sub>, stellar radius; v, rotational velocity; i, stellar inclination; A<sub>b</sub>, Bond albedo.

Johnson–Cousin I filter with an exposure time of 60 s. The photometric data were extracted using the Astrolmagej package<sup>80</sup>.

### GTC/HiPERCAM photometry

A full transit of SPECULOOS-3 b was observed simultaneously (DDT programme GTC2023-216) in five ‘Super’-SDSS filters u<sub>s</sub>, g<sub>s</sub>, r<sub>s</sub>, i<sub>s</sub>, z<sub>s</sub> on 17 September 2023 with the HiPERCAM<sup>81</sup> instrument mounted on the 10.4 m GTC located in the Roque de los Muchachos Observatory in the island of La Palma. The observations covered about 1.94 h centred

around a predicted transit. We reduced the data using the HiPERCAM pipeline, which allowed us to perform aperture photometry with fixed apertures or scaled to the full-width at half-maximum (FWHM) of the individual frames. The set-up that provided the most precise photometry consisted of fixed aperture sizes for the u<sub>s</sub> and z<sub>s</sub> bands, and scaled apertures for the rest. A reference star was constructed by summing the fluxes from four nearby stars in the u<sub>s</sub>, g<sub>s</sub> and r<sub>s</sub> bands, and from one nearby star in the i<sub>s</sub> and z<sub>s</sub> bands. The final light curves showed a clear detection of the transit in all but the u<sub>s</sub> band, in which the target was estimated to have a magnitude of -22.7, and thus the photon noise dominated over the expected transit depth. Additionally, around 6 min after the egress of the transit, a flare was detected in the three bluest bands, with a duration of about 5 min and peak amplitudes of 3%, 9% and 140% in the r<sub>s</sub>, g<sub>s</sub> and u<sub>s</sub> bands, respectively.

### UKIRT photometry

On 27 and 30 August 2023, two transits of SPECULOOS-3 b were observed in the K<sub>s</sub> filter (mean wavelength = 2.2 μm, width = 0.34 μm) with the WFCAM camera on the UKIRT 4 m telescope on Maunakea, Hawaii. Our data analysis started from the calibrated images obtained with the WFCAM detector number 3, which included SPECULOOS-3 and dozens of stars of similar magnitude in its 13.65' × 13.65' field of view. For the first run, the FWHM of the target's point-spread function (PSF) ranged from about 1.5 to 2.75 pixels (WFCAM pixel scale = 0.4"), with a median value of 1.92  $\pm 0.25$  pixels. The PSF was thus poorly sampled in an important part of the images. Despite the active guiding, the x and y positions of the star drifted -1 pixel over the run. The fluxes of the target and comparison stars were measured in the images with IRAF/DAOPHOT<sup>82</sup>. The resulting differential light curves showed substantial correlated noise that we attributed to the FWHM variations, the drift of the stars on the detector and the poor sampling of the PSF. For the second run, the FWHM of the target's PSF ranged from roughly 2.5 to 4.5 pixels, with a median value of 2.69  $\pm 0.53$  pixels. The PSF was thus better sampled than in the first run, resulting in more precise photometry. Here too, the x and y positions of the target drifted -1 pixel along the run.

### CARMENES high-resolution spectroscopy

We observed SPECULOOS-3 with the CARMENES instrument<sup>83</sup> installed at the 3.5 m telescope of Calar Alto Observatory in Almería, Spain. CARMENES has two channels, one in the visible (VIS, 520–960 nm, R = 94,600) and one in the near-infrared (NIR, 960–1,710 nm, R = 80,400). We collected two 1,800 s observations per night (separated by around 3 h) on the four nights between 28 September 2023 and 1 October 2023 and four more observations on 18 and 22 October, 24 November and 8 December 2023. Two of the observations with the NIR channel were not usable due to a problem in one of the NIR detectors on the night of 28 September. The VIS and NIR spectra taken on the night of 22 October were observed during astronomical twilight, meaning that both were contaminated by the solar spectrum. The raw images were reduced using the caracal pipeline<sup>84</sup>. The signal-to-noise ratios ranged around 9 and 30 for the VIS and NIR, respectively. We used Serval<sup>85</sup> to simultaneously determine the vsini<sub>★</sub> (using parameter vsinauto in Serval) and the radial velocities from the VIS spectra. To determine vsini<sub>★</sub> we compared the spectrum of our target with template spectra of stars with various spectral types. Using an M4V template (J11477+008/Ross 128) the single-measurement uncertainties and the radial velocities scatter around the mean were minimized, as compared to using the other templates (M5.5: J00067-075/GJ 1002; M6.0: J07403-174/GJ 283 B; M7.0: J02530+168/Teegarden's star). The vsini<sub>★</sub> estimated with that template was 4.2  $\pm 0.4$  km s<sup>-1</sup>. Assuming that the stellar spin axis aligned to the orbit of planet b, this would result in a rotation period of 1.48  $\pm 0.14$  d. The radial velocities measured from the VIS and NIR spectra have mean uncertainties of 69.0 m s<sup>-1</sup> and 21.9 m s<sup>-1</sup>, respectively. Their analysis discards a slope with an amplitude larger than 5 m s<sup>-1</sup> d<sup>-1</sup> over the two months covered by the CARMENES observations.

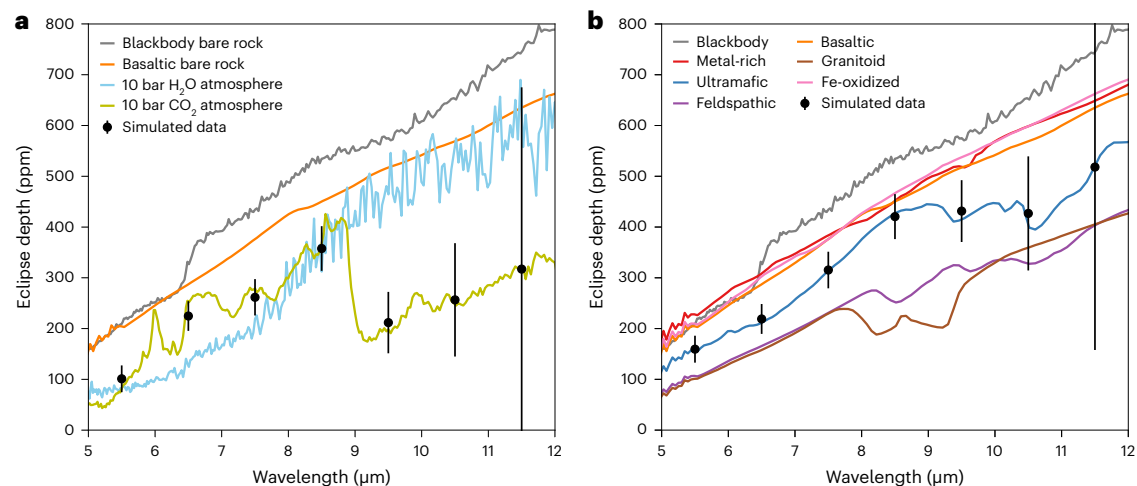


**Fig. 5 | Simulated JWST MIRI/LRS emission spectra of SPECULOOS-3 b.**

**a**, Model emission spectra of SPECULOOS-3 b for two plausible atmospheres and two bare-surface scenarios for comparison. Simulated MIRI/LRS data are shown for the 10 bar CO<sub>2</sub> atmosphere model. **b**, Model emission spectra for a range of surface compositions. Simulated MIRI/LRS data are shown for the ultramafic

surface model as an example. The simulated data were obtained with PandExo<sup>112</sup> assuming ten occultation observations with MIRI/LRS. These data are binned with a constant bin width of 1 μm (average number of points per bin for **a** and **b** = 35) and without any Gaussian scatter around the model, for visual clarity. The error bars are the 1σ errors computed by PandExo.

### High-angular-resolution imaging

SPECULOOS-3 was observed on 4 October 2023 UT using the ‘Alopeke speckle instrument mounted on the Gemini North 8 m telescope<sup>86,87</sup>. ‘Alopeke provides simultaneous speckle imaging in two bands (562 nm and 832 nm) with output data products including a reconstructed image with robust contrast limits on companion detections<sup>88</sup>. Twelve sets of 1,000 × 0.06 s images were obtained and processed in our standard reduction pipeline<sup>89</sup>. Extended Data Fig. 2 shows our final contrast curves and the 832 nm reconstructed speckle image. We found that SPECULOOS-3 is a single star to within the angular and contrast levels achieved with no close companions detected brighter than 5–6 magnitudes below that of the target star from 0.1″ out to 1.2″. At the distance of SPECULOOS-3 ( $d = 16.75$  pc), these angular limits correspond to spatial limits of 1.7 to 20 AU. It is possible to detect companions down to the diffraction limit of Gemini’s 8 m mirror, but with poorer contrast. Equal-brightness companions were excluded at 20 mas (0.34 AU).

Using the Baraffe models<sup>90</sup>,  $\Delta mag = 5$  at 832 nm, the reddest of both bands corresponded to a  $0.071 M_{\odot}$  (74 Jupiter masses  $M_{Jup}$ ) object, at the maximum age inferred for SPECULOOS-3A (8 Gyr). This mass only left sub-stellar objects as plausible companions, unless exactly aligned with the line of sight. If a companion was exactly on the line of sight at the time of observation, it would produce a maximum change in radial velocity. At a distance of 3.4 AU, a  $74 M_{Jup}$  object would produce a radial velocity displacement on SPECULOOS-3A with a stellar semi-amplitude  $K_{*} = 2.8$  km s<sup>-1</sup> over an orbital period  $P \approx 15$  yr. This radial velocity displacement was already refuted by the APOGEE observations.

### Lower limit on the magnitude of a background star

Thanks to the relatively high proper motion of SPECULOOS-3 ( $-0.5''$  yr<sup>-1</sup>), we were able to assess presence of a background star at its current position (RA = 20 h 49 min 27 s, dec = +33° 02′ 35″). We used a 2MASS image<sup>91</sup> obtained in 1998 in the J band. We detected no possible additional source at the current position of SPECULOOS-3. The faintest star in the 2MASS image has a J magnitude of 16.7. We adopted this value as an absolute lower threshold for the J-band magnitude of a background source blended with SPECULOOS-3 in our images obtained with SNO-Artemis telescope. We also compared our current images with Digitized Sky Survey archival images taken more than six decades ago. This comparison (Extended Data Fig. 1) did not reveal any background object at the position of the target.

### Global analysis of the transit photometry

We performed several global analyses of the transit light curves gathered by SPECULOOS, UKIRT/WFCAM, GTC/HiPERCAM and MuSCAT3. These analyses were all done with Traftit, a revised version of the adaptive Markov chain Monte Carlo code presented in refs. 92–94. The model assumed for each light curve was composed of the eclipse model of ref. 95, multiplied by a baseline model aiming to represent the other astrophysical and instrumental mechanisms able to produce photometric variations. For each light curve, the baseline model consisted of a polynomial function of external parameters (for example, time, air-mass,  $x$  and  $y$  positions and so on) selected by minimization of the Bayesian information criterion<sup>96</sup>. In our nominal analysis, the stellar mass  $M_{*}$ , radius  $R_{*}$ , metallicity [Fe/H], parallax  $\pi_{*}$ , effective temperature  $T_{\text{eff}}$  and luminosity  $L_{*}$  were kept under the control of the following prior normal probability distribution functions (PDFs):  $N(0.1017, 0.0024^2) M_{\odot}$ ,  $N(0.123, 0.011^2) R_{\odot}$ ,  $N(0.16, 0.07^2)$  dex,  $N(57.701, 0.043^2)$  mas,  $N(2800, 120^2)$  K and  $N(0.000835, 0.000019^2) L_{\odot}$ , respectively. These prior PDFs reflected our a priori knowledge of the stellar properties (see ‘Host star properties’ above). Given its extremely short orbital period, a circular orbit was assumed for the planet under tidal circularization arguments<sup>97</sup>. A quadratic limb-darkening law<sup>95</sup> was assumed for the star. For the bandpasses  $g'$ ,  $r'$ ,  $i'$ ,  $z'$  and  $K_s$ , values and errors for the linear and quadratic coefficients  $u_1$  and  $u_2$  were derived from the tables of ref. 98, and the corresponding normal distributions were used as prior PDFs in the MCMC (Supplementary Table 2). For the non-standard filter I + z, we adopted the mean value of the  $i'$  and  $z'$  filters for both coefficients. For our three analyses, a preliminary MCMC chain of 50,000 steps was first performed to estimate the need to rescale the photometric errors<sup>93</sup>. A longer MCMC analysis was then performed, composed of two chains of 100,000 steps, whose convergence was checked using the statistical test of ref. 99. In our nominal analysis, we assumed a common transit depth for all bandpasses. The parameters derived from this analysis for the star and its planet are shown in Table 1. Our second analysis assumed different transit depths in each bandpass to check the chromaticity of the transit. The resulting transit depths are shown in Fig. 2. They are all consistent with each other at less than 1σ, a decisive element in the confirmation of the planetary nature of SPECULOOS-3 b. Finally, we performed a third analysis assuming a non-informative uniform prior on the stellar radius and luminosity to obtain an unbiased measurement of the stellar density from the transit photometry alone. It resulted in a stellar density of  $55.1_{-3.7}^{+2.0} \rho_{\odot}$ , in excellent agreement with the density of

$55 \pm 15 \rho_{\odot}$  derived from the a priori knowledge of the star, thus providing further validation of the planetary origin of the transit signals. We also performed individual analyses of the transit light curves to measure the mid-transit timing for each of them (Supplementary Table 3). A linear regression analysis of these timings/epochs did not reveal any significant deviation from a strictly periodic orbit.

### Search for a second planet

Under the arguments presented by ref. 100, we intensively monitored SPECULOOS-3 with SNO-Artemis and MuSCAT3 (data described above) in the hopes of detecting additional transiting planets on longer orbital periods. Our visual inspection of all the gathered light curves did not reveal any convincing additional transit-like structure. After detrending, removal of flares and of transits of SPECULOOS-3 b, we performed a global analysis of all our ground-based light curves with the TLS algorithm<sup>101</sup> that failed to detect any significant power excess indicative of a second transiting planet. We also analysed the flattened TESS light curve with the SHERLOCK package<sup>102</sup>. We found, at first, a strong signal corresponding to the 0.72 d candidate, which allowed us to confirm the detectability of this planet in TESS data (Supplementary Fig. 1). Aside from this signal, we found a few other weaker signals that were all refuted by our ground-based observations. We then performed injection and retrieval experiments on this dataset, which allowed us to establish detection limits. To this end, we used our MATRIX package<sup>102,103</sup>, which generated a sample of synthetic planets by combining a range of orbital periods, planetary radii and orbital phases that were injected in the TESS flattened light curve. In particular, we generated 2,700 scenarios processed in the search for transits using a process that mimicked the SHERLOCK procedure. From the results displayed in Supplementary Fig. 2, we conclude that TESS data allow us to detect Earth-size planets with orbital periods shorter than 1 d. However, the detectability of such small planets rapidly decreases for longer orbital periods, and if they exist and transit, their detection would be very challenging. On the other hand, transiting super-Earth planets with sizes larger than  $1.5 R_{\oplus}$  would be easily detectable with recovery rates ranging from 60–100% for any orbital period up to 10 d, which allowed us to conclude that planets like this do not exist in the system.

### Prospect for mass measurements

Assuming a rocky composition ( $5.5 \pm 0.3 \text{ g cm}^{-3}$ ) for SPECULOOS-3 b, the expected mass would be  $0.93^{+0.12}_{-0.11} M_{\oplus}$ . Its short orbital period (0.72 d) means that SPECULOOS-3 b is expected to produce a radial velocity signal with a semi-amplitude  $K = 3.1 \pm 0.4 \text{ m s}^{-1}$  that should be within reach of state-of-the-art high-resolution high-stability spectrographs mounted on 10-m-class telescopes. To test this hypothesis, we used (1) the empirical relation of late, slowly rotating M dwarfs, obtained as part of the instrumental commissioning of the MAROON-X instrument<sup>104</sup> at the 8.1 m Gemini North telescope (published online at <https://www.gemini.edu>), and (2) the empirical linear dependence of the precision on  $\nu \sin i_{\star}$  (ref. 105) with the CARMENES measurement to estimate that a monitoring campaign of 30–45 MAROON-X spectra should result in a  $3\text{--}4\sigma$  detection of the radial velocity signal of SPECULOOS-3 b and, hence, to a first measurement of its mass.

### The JWST emission opportunity

Measuring the emission spectrum of an exoplanet is typically harder than measuring its transmission spectrum. However, emission comes with advantages that overall make it a robust method to study an exoplanet. In particular, emission spectra are not affected by stellar photospheric heterogeneity. Indeed, in transit, the average stellar spectrum over the transit chord can differ from the rest of the photosphere because of heterogeneities leading to spurious spectral features in the transmission spectrum<sup>36,106,107</sup>. As expected, this effect is observed in the case of TRAPPIST-1 b (part of GO 1281 (ref. 31)), which makes inferring an atmosphere for the TRAPPIST-1 planets a challenging task. UDS are also

known to be magnetically active with frequent flaring (confirmed from the TESS light curves and ground-based photometric observations). Unfortunately, this can be damaging for transmission spectroscopy as frequent flares visible in the NIR can affect the shape of the eclipses and the retrieval of the planet's parameters (see recommendations in ref. 31 about the TRAPPIST-1 b transit spectrum). Luckily, the contrast of flares drops with longer wavelengths and their mid-IR counterpart should impact the light curves much less. Emission spectroscopy has other advantages over transmission spectroscopy. First, the interpretation of emission spectra is not dependent on the mass of the planet. Second, emission spectra provide the energy budget of the planet, which is essential to understanding its atmosphere's chemistry and its dynamics, and can be used to constrain the planet's albedo. Finally, in the absence of an atmosphere, emission spectroscopy instead directly accesses the planetary surface where its mineralogy can be studied, something that is impossible to achieve with transmission spectroscopy. For all these reasons, emission spectroscopy is a more reliable method to assess the presence of an atmosphere and study the nature of terrestrial planets around UDS. And, as shown on Fig. 4b, SPECULOOS-3 b is one of the smallest terrestrial planets that is within reach of JWST in emission spectroscopy with MIRI/LRS. We therefore modelled plausible atmospheric and surface scenarios and compared them to realistic simulations of MIRI/LRS observations of SPECULOOS-3 b in emission.

### Model emission spectra

We first modelled the emission spectra of SPECULOOS-3 b assuming  $\text{CO}_2$ -dominated and  $\text{H}_2\text{O}$ -dominated atmospheres, which are among the most plausible atmospheric composition families for hot, rocky planets<sup>28</sup>. To do this, we performed 3D global climate model calculations using the state-of-the-art Generic Planetary Climate Model<sup>108,109</sup>. The model includes self-consistent treatment of radiation, convection and clouds. Parameterizations of these processes are detailed in ref. 109. In short, radiation is computed by the correlated- $k$  approach, using opacity tables based on the High-resolution TRANsmission molecular absorption and High-TEMPerature molecular spectroscopic databases; convection is represented through dry and moist adjustment schemes;  $\text{H}_2\text{O}$  and  $\text{CO}_2$  cloud formation is treated using a prognostic scheme, and assumes a fixed amount of cloud condensation nuclei. Simulations showed a strong temperature inversion in the stratosphere, as well as a strong day–night temperature contrast, affecting the emission spectra (Fig. 5a). Although the global climate model included cloud formation, no  $\text{H}_2\text{O}$  or  $\text{CO}_2$  clouds formed in these simulations due to the high irradiation the planet receives, which reduces the planet's albedo and thus increases its thermal emission. We then modelled the theoretical emission spectrum of an airless planet with a null albedo and the absence of heat redistribution by considering the planetary flux to be a sum of black bodies calculated for a grid of  $T_{\theta,\phi}$ , where  $\theta$  and  $\phi$  are the longitude and the latitude, respectively. The temperature of the sub-stellar point (at zenith) was chosen to be the maximal dayside temperature defined as  $T_{\text{day,max}} = T_{\star} \times \sqrt{\frac{R_{\star}}{a}} \times \left(\frac{2}{3}\right)^{1/4}$ , where  $a$  is the planet's semi-major axis. The temperature then decreased with increasing latitude and longitude. In addition to this simple blackbody model, we modelled emission spectra for several geologically plausible planetary surface types, including ultramafic crust formed from the solidification of a magma ocean or high-temperature lava flows, basaltic crust that formed from volcanic eruptions like those on present-day Earth and granitoid crust formed from crustal reprocessing. The data for different surfaces were based on single scattering albedos derived in ref. 110. An ultramafic crust and a granitoid crust would be mainly composed of silicates that have intense spectral features between 8 and  $12 \mu\text{m}$  due to Si–O stretching<sup>110</sup>, and these features are detectable with MIRI/LRS observations (see PandExo simulations below and Fig. 5b). In addition to searching for spectral features, emission spectroscopy can also constrain the



planet's dayside albedo and thus its geological history. In the Solar System, airless bare rocks like the Moon and Mercury are much darker than fresh geologic surfaces due to the effect of space weathering<sup>38</sup>. If SPECULOOS-3 b is an airless rocky planet, then we would similarly expect its surface to become progressively darker. We performed simulations of this effect by considering the albedo effect of graphite particles on a fresh ultramafic surface, using the same approach followed in ref. 111. We found that even moderate space weathering would substantially lower the dayside albedo, thereby increasing the planet's brightness temperature (and thus eclipse depth) at MIRI/LRS wavelengths (Extended Data Fig. 4). For reference, the space weathering timescale on TRAPPIST-1 c was estimated to be  $10^2$ – $10^3$  yr (ref. 33); given their similar planetary and stellar parameters, the space weathering timescale for SPECULOOS-3 b should be of a similar order of magnitude. Any detection of a high-albedo dayside would thus require that the planet's surface is geologically very young, indicating that the planet has a very active volcanism or tectonic overturn.

### PandExo simulations

We used the PandExo<sup>112</sup> simulation tool to estimate the noise of a single secondary eclipse observation of SPECULOOS-3 b with MIRI/LRS in slitless spectroscopy mode. For the stellar spectrum, we used the best-fit PHOENIX model from our SED fitting (see above), normalized to  $a/mag = 11.501$ . We assumed 180 groups per integration to optimize the observing efficiency (~99%), while keeping the counts level below 90% saturation according to JWST Exposure Time Calculator. This yielded a total time per integration (including readout and reset) of 28.63 s. We set the total observing time to 2.9 h. This duration took into account a margin of 1 h for the start of the observations, 30 min for the stabilization of the detector, 28 min of baseline before the start of the eclipse, 28 min during the eclipse and 28 min of baseline after the eclipse. Finally, we assumed a systematic noise floor of 30 ppm based on the performances reported from previous observations (for example, ref. 113). We then tested how many secondary eclipse observations would be necessary to distinguish different models from one another, following an approach similar to that of ref. 114. For each pair of models, we conducted a chi-square test and obtained a  $P$  value representing the probability that the simulated data from the model to be tested were consistent with the second model. For each simulated dataset, we used the PandExo output that included a random Gaussian noise component ('spectrum\_w\_rand' key in the output file). We started with one eclipse and increased the number of eclipses until the two models were distinguishable by  $4\sigma$ , corresponding to a  $P$  value of less than 0.000063. We conducted these tests using a variety of wavelength bins, either of constant resolution  $R$  ( $\lambda/\Delta\lambda$ ) or constant width ( $\Delta\lambda$ ). We found that the models were maximally distinguishable for a resolution  $R = 3$  in the first case, or a bin width =  $2 \mu\text{m}$  in the second case. Extended Data Table 1 shows the number of secondary eclipse observations needed to distinguish the  $\text{CO}_2$  and  $\text{H}_2\text{O}$  atmospheric models from two common airless planet models (blackbody and basaltic) at  $4\sigma$ . At most, seven eclipses were needed to assess the presence of the most plausible atmosphere for SPECULOOS-3 b with  $4\sigma$  confidence. Extended Data Table 2 also shows that observing two additional occultations, that is, nine occultations in total, should allow one to distinguish a  $\text{CO}_2$ -dominated atmosphere from an  $\text{H}_2\text{O}$ -dominated one. Should there be no evidence for an atmosphere, the MIRI/LRS emission spectrum could be used to assess different surface compositions. Extended Data Table 2 reports the number of secondary eclipse observations needed to distinguish different surface models at  $4\sigma$ . About 50% of the considered surface pairs should be distinguishable at  $\geq 4\sigma$  with ten eclipse observations.

### Data availability

All the data (Kast, SpeX and CARMENES spectra; SPECULOOS, Saint-EX, T150, MuSCAT3, GTC/HiPERCAM, UKIRT/WFCAM and TESS light curves) used in this work are publicly available via Zenodo at

<https://doi.org/10.5281/zenodo.10821723> (ref. 115). Source data are provided with this paper.

### Code availability

The PROSE code used to reduce the SPECULOOS, TRAPPIST, and MuSCAT3 data is available at <https://github.com/lgrcia/prose>. The TRAFIT code used to analyse the light curves is a Fortran2003 code that can be obtained from the first author on reasonable request. The HiPERCAM pipeline is available at <https://cygnus.astro.warwick.ac.uk/phsaap/hipercam/docs/html/>. The SHERLOCK package used to search for planets in the TESS data is publicly available at <https://github.com/franpoz/SHERLOCK>. The detection limits in the TESS data were computed using the MATRIX package, which is publicly available at <https://github.com/PlanetHunters/tkmatrix>. The code used to create Extended Data Fig. 1 is available at <https://github.com/jpdeleon/epoch>. The Generic Planetary Climate Model code (and documentation on how to use the model) used in this work can be downloaded from the SVN repository at <https://svn.lmd.jussieu.fr/Planeto/trunk/LMDZ.GENERIC/>. The Donuts code is available at <https://github.com/jmccormac01/Donuts>. More information and documentation are available at <http://www.planets.lmd.jussieu.fr>. The kastredux code used to reduce the Kast optical spectrum is available at <https://github.com/aburgasser/kastredux>.

### References

1. Kirkpatrick, J. D., Henry, T. J. & Irwin, M. J. Ultra-cool M dwarfs discovered by QSO surveys. I: the APM objects. *Astron. J.* **113**, 1421–1428 (1997).
2. Dieterich, S. B. et al. The solar neighborhood. XXXII. The hydrogen burning limit. *Astron. J.* **147**, 94 (2014).
3. Gillon, M. Searching for red worlds. *Nat. Astron.* **2**, 344 (2018).
4. Burdanov, A., Delrez, L., Gillon, M. & Jehin, E. in *Handbook of Exoplanets* (eds Deeg, H. J. & Belmonte, J. A.) 1007–1023 (Springer, 2018).
5. Delrez, L. et al. SPECULOOS: a network of robotic telescopes to hunt for terrestrial planets around the nearest ultracool dwarfs. In *Proc. SPIE 10700, Ground-Based and Airborne Telescopes VII* (eds Marshall, H. K. & Spyromilio, J.) 107001I (SPIE, 2018).
6. Sebastian, D. et al. SPECULOOS: ultracool dwarf transit survey. Target list and strategy. *Astron. Astrophys.* **645**, A100 (2021).
7. Jehin, E. et al. The SPECULOOS Southern Observatory begins its hunt for rocky planets. *Messenger* **174**, 2–7 (2018).
8. Burdanov, A. Y. et al. SPECULOOS Northern Observatory: searching for red worlds in the northern skies. *Publ. Astron. Soc. Pac.* **134**, 105001 (2022).
9. Demory, B. O. et al. A super-Earth and a sub-Neptune orbiting the bright, quiet M3 dwarf TOI-1266. *Astron. Astrophys.* **642**, A49 (2020).
10. Gillon, M., Jehin, E., Fumel, A., Magain, P. & Queloz, D. TRAPPIST-UCDTS: a prototype search for habitable planets transiting ultra-cool stars. *EPJ Web Conf.* **47**, 03001 (2013).
11. Gillon, M. et al. Temperate Earth-sized planets transiting a nearby ultracool dwarf star. *Nature* **533**, 221–224 (2016).
12. Gillon, M. et al. Seven temperate terrestrial planets around the nearby ultracool dwarf star TRAPPIST-1. *Nature* **542**, 456–460 (2017).
13. Delrez, L. et al. Two temperate super-Earths transiting a nearby late-type M dwarf. *Astron. Astrophys.* **667**, A59 (2022).
14. Stassun, K. G., Corsaro, E., Pepper, J. A. & Gaudi, B. S. Empirical accurate masses and radii of single stars with TESS and Gaia. *Astron. J.* **155**, 22 (2018).
15. Birky, J., Hogg, D. W., Mann, A. W. & Burgasser, A. Temperatures and metallicities of M dwarfs in the APOGEE Survey. *Astrophys. J.* **892**, 31 (2020).
16. Stelzer, B., Marino, A., Micela, G., López-Santiago, J. & Liefke, C. The UV and X-ray activity of the M dwarfs within 10 pc of the Sun. *Mon. Not. R. Astron. Soc.* **431**, 2063–2079 (2013).

17. Lopez, E. D., Fortney, J. J. & Miller, N. How thermal evolution and mass-loss sculpt populations of super-Earths and sub-Neptunes: application to the Kepler-11 system and beyond. *Astrophys. J.* **761**, 59 (2012).
18. Owen, J. E. & Mohanty, S. Habitability of terrestrial-mass planets in the HZ of M Dwarfs - I. H/He-dominated atmospheres. *Mon. Not. R. Astron. Soc.* **459**, 4088–4108 (2016).
19. Owen, J. E. & Wu, Y. Kepler planets: a tale of evaporation. *Astrophys. J.* **775**, 105 (2013).
20. Owen, J. E. & Wu, Y. The evaporation valley in the Kepler planets. *Astrophys. J.* **847**, 29 (2017).
21. Fulton, B. J. et al. The California-Kepler Survey. III. A gap in the radius distribution of small planets. *Astron. J.* **154**, 109 (2017).
22. Luque, R. & Pallé, E. Density, not radius, separates rocky and water-rich small planets orbiting M dwarf stars. *Science* **377**, 1211–1214 (2022).
23. Petigura, E. A. et al. The California-Kepler Survey. X. The radius gap as a function of stellar mass, metallicity, and age. *Astron. J.* **163**, 179 (2022).
24. Akeson, R. L. et al. The NASA Exoplanet Archive: data and tools for exoplanet research. *Publ. Astron. Soc. Pac.* **125**, 989 (2013).
25. Izidoro, A. et al. Breaking the chains: hot super-Earth systems from migration and disruption of compact resonant chains. *Mon. Not. R. Astron. Soc.* **470**, 1750–1770 (2017).
26. Izidoro, A. et al. Formation of planetary systems by pebble accretion and migration. Hot super-Earth systems from breaking compact resonant chains. *Astron. Astrophys.* **650**, A152 (2021).
27. Goldberg, M. & Batygin, K. Architectures of compact super-Earth systems shaped by instabilities. *Astron. J.* **163**, 201 (2022).
28. Forget, F. & Leconte, J. Possible climates on terrestrial exoplanets. *Phil. Trans. R. Soc. A* **372**, 20130084 (2014).
29. Zahnle, K. J. & Catling, D. C. The cosmic shoreline: the evidence that escape determines which planets have atmospheres, and what this may mean for Proxima Centauri B. *Astrophys. J.* **843**, 122 (2017).
30. Grenfell, J. L. et al. Possible atmospheric diversity of low mass exoplanets - some central aspects. *Space Sci. Rev.* **216**, 98 (2020).
31. Lim, O. et al. Atmospheric reconnaissance of TRAPPIST-1 b with JWST/NIRISS: evidence for strong stellar contamination in the transmission spectra. *Astrophys. J. Lett.* **955**, L22 (2023).
32. Greene, T. P. et al. Thermal emission from the Earth-sized exoplanet TRAPPIST-1 b using JWST. *Nature* **618**, 39–42 (2023).
33. Zieba, S. et al. No thick carbon dioxide atmosphere on the rocky exoplanet TRAPPIST-1 c. *Nature* **620**, 746–749 (2023).
34. Mansfield, M. et al. Identifying atmospheres on rocky exoplanets through inferred high albedo. *Astrophys. J.* **886**, 141 (2019).
35. Kempton, E. M.-R. et al. A framework for prioritizing the TESS planetary candidates most amenable to atmospheric characterization. *Publ. Astron. Soc. Pac.* **130**, 114401 (2018).
36. Rackham, B. V., Apai, D. & Giampapa, M. S. The transit light source effect: false spectral features and incorrect densities for M-dwarf transiting planets. *Astrophys. J.* **853**, 122 (2018).
37. May, E. M. et al. Double trouble: two transits of the super-Earth GJ 1132 b observed with JWST NIRSpec G395H. *Astrophys. J. Lett.* **959**, L9 (2023).
38. Hapke, B. Space weathering from Mercury to the asteroid belt. *J. Geophys. Res.* **106**, 10039–10074 (2001).
39. Lépine, S. & Shara, M. M. A catalog of northern stars with annual proper motions larger than 0.15" (LSPM-NORTH Catalog). *Astron. J.* **129**, 1483–1522 (2005).
40. Dittmann, J. A., Irwin, J. M., Charbonneau, D. & Berta-Thompson, Z. K. Trigonometric parallaxes for 1507 nearby mid-to-late M dwarfs. *Astrophys. J.* **784**, 156 (2014).
41. Gilhool, S. H. et al. The rotation of M dwarfs observed by the Apache Point Galactic Evolution Experiment. *Astron. J.* **155**, 38 (2018).
42. Jönsson, H. et al. APOGEE data and spectral analysis from SDSS Data Release 16: seven years of observations including first results from APOGEE-South. *Astron. J.* **160**, 120 (2020).
43. Gaia Collaboration. Gaia Data Release 2. Summary of the contents and survey properties. *Astron. Astrophys.* **616**, A1 (2018).
44. Scholz, R. D. New ultracool dwarf neighbours within 20 pc from Gaia DR2. *Astron. Astrophys.* **637**, A45 (2020).
45. Rayner, J. T. et al. SpeX: a medium-resolution 0.8–5.5 micron spectrograph and imager for the NASA Infrared Telescope Facility. *Publ. Astron. Soc. Pac.* **115**, 362–382 (2003).
46. Cushing, M. C., Vacca, W. D. & Rayner, J. T. Spextool: a spectral extraction package for SpeX, a 0.8–5.5 micron cross-dispersed spectrograph. *Publ. Astron. Soc. Pac.* **116**, 362–376 (2004).
47. Burgasser, A. J. & Splat Development Team. The SpeX Prism Library Analysis Toolkit (SPLAT): a data curation model. In *3rd International Workshop on Spectral Stellar Libraries, Astronomical Society of India Conference* (eds Coelho, P. et al.) 7–12 (Astronomical Society of India, 2017).
48. Cushing, M. C., Rayner, J. T. & Vacca, W. D. An infrared spectroscopic sequence of M, L, and T dwarfs. *Astron. J.* **623**, 1115–1140 (2005).
49. Rayner, J. T., Cushing, M. C. & Vacca, W. D. The Infrared Telescope Facility (IRTF) spectral library: cool stars. *Astrophys. J. Suppl. Ser.* **185**, 289–432 (2009).
50. Kirkpatrick, J. D. et al. Discoveries from a near-infrared proper motion survey using multi-epoch two micron All-Sky Survey data. *Astrophys. J. Suppl. Ser.* **190**, 100–146 (2010).
51. Mann, A. W. et al. Prospecting in ultracool dwarfs: measuring the metallicities of mid- and late-M dwarfs. *Astron. J.* **147**, 160 (2014).
52. Miller, J. S. & Stone, R. P. S. *The Kast Double Spectrograph* Technical Report No. 66 (Univ. California Lick Observatory, 1994).
53. Kesseli, A. Y. et al. An empirical template library of stellar spectra for a wide range of spectral classes, luminosity classes, and metallicities using SDSS BOSS spectra. *Astrophys. J. Suppl. Ser.* **230**, 16 (2017).
54. Gizis, J. E. M-subdwarfs: spectroscopic classification and the metallicity scale. *Astron. J.* **113**, 806–822 (1997).
55. Martín, E. L. et al. Spectroscopic classification of late-M and L field dwarfs. *Astron. J.* **118**, 2466–2482 (1999).
56. Lépine, S., Rich, R. M. & Shara, M. M. Spectroscopy of new high proper motion stars in the northern sky. I. New nearby stars, new high-velocity stars, and an enhanced classification scheme for M dwarfs. *Astron. J.* **125**, 1598–1622 (2003).
57. Lépine, S. et al. A spectroscopic catalog of the brightest ( $J < 9$ ) M dwarfs in the northern sky. *Astron. J.* **145**, 102 (2013).
58. Mann, A. W., Brewer, J. M., Gaidos, E., Lépine, S. & Hilton, E. J. Prospecting in late-type dwarfs: a calibration of infrared and visible spectroscopic metallicities of late K and M dwarfs spanning 1.5 dex. *Astron. J.* **145**, 52 (2013).
59. Stassun, K. G. & Torres, G. Parallax systematics and photocenter motions of benchmark eclipsing binaries in Gaia EDR3. *Astrophys. J. Lett.* **907**, L33 (2021).
60. Stassun, K. G. & Torres, G. Eclipsing binaries as benchmarks for trigonometric parallaxes in the Gaia era. *Astron. J.* **152**, 180 (2016).
61. Stassun, K. G., Collins, K. A. & Gaudi, B. S. Accurate empirical radii and masses of planets and their host stars with Gaia parallaxes. *Astron. J.* **153**, 136 (2017).
62. Husser, T. O. et al. A new extensive library of PHOENIX stellar atmospheres and synthetic spectra. *Astron. Astrophys.* **553**, A6 (2013).
63. Filippazzo, J. C. et al. Fundamental parameters and spectral energy distributions of young and field age objects with masses spanning the stellar to planetary regime. *Astrophys. J.* **810**, 158 (2015).

64. Mann, A. W. et al. How to constrain your M dwarf. II. The mass-luminosity-metallicity relation from 0.075 to 0.70 solar masses. *Astrophys. J.* **871**, 63 (2019).
65. Czesla, S. et al. PyA: Python astronomy-related packages. *Astrophysics Source Code Library* ascl:1906.010 (2019).
66. Johnson, D. R. H. & Soderblom, D. R. Calculating galactic space velocities and their uncertainties, with an application to the Ursa Major group. *Astron. J.* **93**, 864 (1987).
67. Gaia Collaboration. Gaia Early Data Release 3. Summary of the contents and survey properties. *Astron. Astrophys.* **649**, A1 (2021).
68. Coşkunoğlu, B. et al. Local stellar kinematics from RAVE data - I. Local standard of rest. *Mon. Not. R. Astron. Soc.* **412**, 1237–1245 (2011).
69. Li, C. & Zhao, G. The evolution of the galactic thick disk with the LAMOST Survey. *Astrophys. J.* **850**, 25 (2017).
70. Buder, S. et al. The GALAH+ survey: third data release. *Mon. Not. R. Astron. Soc.* **506**, 150–201 (2021).
71. Fernandes, C. S. et al. Evolutionary models for ultracool dwarfs. *Astrophys. J.* **879**, 94 (2019).
72. Lightkurve Collaboration et al. Lightkurve: Kepler and TESS time series analysis in Python. *Astrophysics Source Code Library* ascl:1812.013 (2018).
73. Narita, N. et al. MuSCAT2: four-color simultaneous camera for the 1.52-m Telescopio Carlos Sánchez. *J. Astron. Telesc. Instrum. Syst.* **5**, 015001 (2019).
74. Narita, N. et al. MuSCAT3: a 4-color simultaneous camera for the 2m Faulkes Telescope North. In *Proc. Ground-based and Airborne Instrumentation for Astronomy VIII* (eds Evans, C. J. et al.) 114475K (SPIE, 2020).
75. McCully, C. et al. in *Software and Cyberinfrastructure for Astronomy V Conference Series Vol. 10707* (eds Guzman, J. C. & Ibsen, J.) 107070K (SPIE, 2018).
76. Garcia, L. J. et al. PROSE: a PYTHON framework for modular astronomical images processing. *Mon. Not. R. Astron. Soc.* **509**, 4817–4828 (2022).
77. Gillon, M. et al. TRAPPIST: a robotic telescope dedicated to the study of planetary systems. *EPJ Web Conf.* **11**, 06002 (2011).
78. Jehin, E. et al. TRAPPIST: transiting planets and planetesimals small telescope. *Messenger* **145**, 2–6 (2011).
79. Barkaoui, K. et al. Discovery of three new transiting hot Jupiters: WASP-161 b, WASP-163 b, and WASP-170 b. *Astron. J.* **157**, 43 (2019).
80. Collins, K. A., Kielkopf, J. F., Stassun, K. G. & Hessman, F. V. AstrolmageJ: image processing and photometric extraction for ultra-precise astronomical light curves. *Astron. J.* **153**, 77 (2017).
81. Dhillon, V. S. et al. HiPERCAM: a quintuple-beam, high-speed optical imager on the 10.4-m Gran Telescopio Canarias. *Mon. Not. R. Astron. Soc.* **507**, 350–366 (2021).
82. Stetson, P. B. DAOPHOT: a computer program for crowded-field stellar photometry. *Publ. Astron. Soc. Pac.* **99**, 191 (1987).
83. Quirrenbach, A. et al. The CARMENES M-dwarf planet survey. In *Proc. SPIE 11447, Ground-based and Airborne Instrumentation for Astronomy VIII* (eds Evans, C. J. et al.) 114473C (SPIE, 2020).
84. Caballero, J. A. et al. in *Observatory Operations: Strategies, Processes, and Systems VI Conference Series Vol. 9910* (eds Peck, A. B. et al.) 99100E (SPIE, 2016).
85. Zechmeister, M. et al. Spectrum radial velocity analyser (SERVAL). High-precision radial velocities and two alternative spectral indicators. *Astron. Astrophys.* **609**, A12 (2018).
86. Scott, N. J. et al. Twin high-resolution, high-speed imagers for the Gemini telescopes: instrument description and science verification results. *Front. Astron. Space Sci.* **8**, 138 (2021).
87. Howell, S. B. & Furlan, E. Speckle interferometric observations with the Gemini 8-m telescopes: signal-to-noise calculations and observational results. *Front. Astron. Space Sci.* **9**, 871163 (2022).
88. Howell, S. B. et al. Speckle imaging excludes low-mass companions orbiting the exoplanet host star TRAPPIST-1. *Astrophys. J. Lett.* **829**, L2 (2016).
89. Howell, S. B., Everett, M. E., Sherry, W., Horch, E. & Ciardi, D. R. Speckle camera observations for the NASA Kepler Mission follow-up program. *Astron. J.* **142**, 19 (2011).
90. Baraffe, I., Homeier, D., Allard, F. & Chabrier, G. New evolutionary models for pre-main sequence and main sequence low-mass stars down to the hydrogen-burning limit. *Astron. Astrophys.* **577**, A42 (2015).
91. Skrutskie, M. F. et al. The Two Micron All Sky Survey (2MASS). *Astron. J.* **131**, 1163–1183 (2006).
92. Gillon, M. et al. The Spitzer search for the transits of HARPS low-mass planets. I. No transit for the super-Earth HD 40307b. *Astron. Astrophys.* **518**, A25 (2010).
93. Gillon, M. et al. The TRAPPIST survey of southern transiting planets. I. Thirty eclipses of the ultra-short period planet WASP-43 b. *Astron. Astrophys.* **542**, A4 (2012).
94. Gillon, M. et al. Search for a habitable terrestrial planet transiting the nearby red dwarf GJ 1214. *Astron. Astrophys.* **563**, A21 (2014).
95. Mandel, K. & Agol, E. Analytic light curves for planetary transit searches. *Astrophys. J. Lett.* **580**, L171–L175 (2002).
96. Schwarz, G. Estimating the dimension of a model. *Ann. Stat.* **6**, 461–464 (1978).
97. Matsumura, S., Takeda, G. & Rasio, F. A. On the origins of eccentric close-in planets. *Astrophys. J. Lett.* **686**, L29 (2008).
98. Claret, A., Hauschildt, P. H. & Witte, S. New limb-darkening coefficients for PHOENIX/1D model atmospheres. I. Calculations for  $1500\text{ K} \leq T_{\text{eff}} \leq 4800\text{ K}$  Kepler, CoRot, Spitzer, uvby, UVRIJHK, Sloan, and 2MASS photometric systems. *Astron. Astrophys.* **546**, A14 (2012).
99. Gelman, A. & Rubin, D. B. Inference from iterative simulation using multiple sequences. *Stat. Sci.* **7**, 457–472 (1992).
100. Gillon, M. et al. An educated search for transiting habitable planets: targeting M dwarfs with known transiting planets. *Astron. Astrophys.* **525**, A32 (2011).
101. Hippke, M. & Heller, R. Optimized transit detection algorithm to search for periodic transits of small planets. *Astron. Astrophys.* **623**, A39 (2019).
102. Pozuelos, F. J. et al. GJ 273: on the formation, dynamical evolution, and habitability of a planetary system hosted by an M dwarf at 3.75 parsec. *Astron. Astrophys.* **641**, A23 (2020).
103. Dévora-Pajares, M. & Pozuelos, F. J. MATRIX: multi-phase transits recovery from injected exoplanets toolkit. *Astrophysics Source Code Library* ascl:2309.007 (2023).
104. Seifahrt, A. et al. On-sky commissioning of MAROON-X: a new precision radial velocity spectrograph for Gemini North. In *Proc. SPIE 11447, Ground-based and Airborne Instrumentation for Astronomy VIII* (eds Evans, C. J. et al.) 114471F (SPIE, 2020).
105. Hatzes, A. P., Cochran, W. D. & Endl, M. in *Planets in Binary Star Systems Astrophysics and Space Science Library* Vol. 366 (ed Haghhighipour, N.) 51–76 (Astrophysics and Space Science Library, 2010).
106. Rackham, B. V., Apai, D. & Giampapa, M. S. The transit light source effect. II. The impact of stellar heterogeneity on transmission spectra of planets orbiting broadly Sun-like stars. *Astron. J.* **157**, 96 (2019).
107. Rackham, B. V. et al. The effect of stellar contamination on low-resolution transmission spectroscopy: needs identified by NASA's Exoplanet Exploration Program Study Analysis Group 21. *RAS Techniq. Instrum.* **2**, 148–206 (2023).
108. Leconte, J. et al. 3D climate modeling of close-in land planets: circulation patterns, climate moist bistability, and habitability. *Astron. Astrophys.* **554**, A69 (2013).

109. Turbet, M. et al. Water condensation zones around main sequence stars. *Astron. Astrophys.* **679**, A126 (2023).
110. Hu, R., Ehlmann, B. L. & Seager, S. Theoretical spectra of terrestrial exoplanet surfaces. *Astrophys. J.* **752**, 7 (2012).
111. Lyu, X. et al. Super-Earth LHS3844b is tidally locked. *Astrophys. J.* **964**, 152 (2024).
112. Batalha, N. E. et al. PandExo: a community tool for transiting exoplanet science with JWST & HST. *Publ. Astron. Soc. Pac.* **129**, 064501 (2017).
113. Bouwman, J. et al. Spectroscopic time series performance of the mid-infrared instrument on the JWST. *Publ. Astron. Soc. Pac.* **135**, 038002 (2023).
114. Whittaker, E. A. et al. The detectability of rocky planet surface and atmosphere composition with the JWST: the case of LHS 3844b. *Astron. J.* **164**, 258 (2022).
115. Gillon, M. Detection of an Earth-sized exoplanet orbiting the nearby ultracool dwarf star SPECULOOS-3. *Zenodo* <https://doi.org/10.5281/zenodo.10821723> (2024).
116. *NASA Exoplanet Archive* (California Institute of Technology, accessed 16 October 2023); <https://exoplanetarchive.ipac.caltech.edu>

## Acknowledgements

The ULiege's contribution to SPECULOOS has received funding from the European Research Council under the European Union's Seventh Framework Programme (FP/2007-2013) (grant agreement number 336480/SPECULOOS), the Balzan Prize and Francqui Foundations, the Belgian Scientific Research Foundation (F.R.S.-FNRS; grant number T.0109.20), the University of Liege and the ARC grant for Concerted Research Actions financed by the Wallonia-Brussels Federation. M. Gillon is an F.R.S.-FNRS Research Director. His contribution to this work was done in the framework of the PORTAL project funded by the Federal Public Planning Service Science Policy (BELSPO) within its BRAIN-be: Belgian Research Action through Interdisciplinary Networks programme. E.J. is an F.R.S.-FNRS Senior Research Associate. V.V.G. is an F.R.S.-FNRS Research Associate. The postdoctoral fellowship of K.B. is funded by F.R.S.-FNRS grant number T.0109.20 and by the Francqui Foundation. This publication benefits from the support of the French Community of Belgium in the context of the FRIA Doctoral Grant awarded to M. Timmermans. This work is supported by a grant from the Simons Foundation (PI D.Q., grant number 327127). J.d.W. and MIT gratefully acknowledge financial support from the Heising-Simons Foundation, C. Masson and L. Masson and P. A. Gilman for Artemis, the first telescope of the SPECULOOS network situated in Tenerife, Spain. B.-O.D. acknowledges support from the Centre for Space and Habitability of the University of Bern and the Swiss State Secretariat for Education, Research and Innovation (SERI) under contract number MB22.00046. Part of this work received support from the National Centre for Competence in Research PlanetS, supported by the Swiss National Science Foundation (SNSF). The Birmingham contribution research is in part funded by the European Union's Horizon 2020 research and innovation programme (grant agreement number 803193/BEBOP), from the MERAC foundation and from the Science and Technology Facilities Council (STFC; grant numbers ST/SO0193X/1 and ST/W000385/1). We thank the Belgian Federal Science Policy Office (BELSPO) for the provision of financial support in the framework of the PRODEX Programme of the European Space Agency (ESA) under contract number 4000142531. B.V.R. thanks the Heising-Simons Foundation for Support. B.V.R. is a 51 Pegasi b Fellow. This material is based upon work supported by the National Aeronautics and Space Administration under agreement number 80NSSC21K0593 for the programme 'Alien Earths'. The results reported herein benefited from collaborations and/or information exchange within NASA's Nexus for Exoplanet System Science (NExSS) research coordination network sponsored by NASA's Science Mission Directorate. M. Turbet acknowledges support from the Tremplin 2022

programme of the Faculty of Science and Engineering of Sorbonne University. M. Turbet thanks the Generic PCM team for the teamwork development and improvement of the model and acknowledges support from the High-Performance Computing (HPC) resources of Centre Informatique National de l'Enseignement Supérieur (CINES) under the allocation numbers A0100110391, A0120110391 and A0140110391 made by Grand Équipement National de Calcul Intensif (GENCI). M.R.S acknowledges support from the European Space Agency as an ESA Research Fellow. E.A.M.V. acknowledges support from the Centre for Space and Habitability (CSH). This work has been carried out within the framework of the National Centre of Competence in Research PlanetS supported by the Swiss National Science Foundation under grant numbers 51NF40\_182901 and 51NF40\_205606. This work is based upon observations carried out at the Observatorio Astronómico Nacional on the Sierra de San Pedro Mártir (OAN-SPM), Baja California, México. SAINT-EX observations and team were supported by the Swiss National Science Foundation (grant numbers PPO0P2-163967 and PPO0P2-190080), the Centre for Space and Habitability (CSH) of the University of Bern and the National Centre for Competence in Research PlanetS, supported by the SNSF. Y.G.M.C. acknowledges support from UNAM PAPIIT-IG101224. Based on observations made with the GTC telescope, in the Spanish Observatorio del Roque de los Muchachos of the Instituto de Astrofísica de Canarias, under Director's Discretionary Time. Some of the observations in this paper made use of the High-Resolution Imaging instrument 'Alopeke and were obtained under Gemini LLP proposal number GN-2023B-DD-101. 'Alopeke was funded by the NASA Exoplanet Exploration Program and built at the NASA Ames Research Center by S.B.H., N. Scott, E. P. Horch and E. Quigley. 'Alopeke was mounted on the Gemini North telescope of the international Gemini Observatory, a programme of the NSF's OIR Lab, which is managed by the Association of Universities for Research in Astronomy (AURA) under a cooperative agreement with the National Science Foundation on behalf of the Gemini partnership: the National Science Foundation (United States), National Research Council (Canada), Agencia Nacional de Investigación y Desarrollo (Chile), Ministerio de Ciencia, Tecnología e Innovación (Argentina), Ministério da Ciência, Tecnologia, Inovações e Comunicações (Brazil) and Korea Astronomy and Space Science Institute (Republic of Korea). F.J.P., P.J.A., A.S., R.V., and J.A. acknowledge financial support from the Severo Ochoa grant CEX2021-001131-S funded by the Spanish Ministry of Science and Innovation grant MCIN/AEI/10.13039/501100011033. This work benefited from observations made at the Sierra Nevada Observatory, operated by the Instituto de Astrofísica de Andalucía (IAA-CSIC). D.K. and X.L. acknowledge financial support from NSFC grant number 42250410318. F.S. acknowledges support from CNES, Programme National de Planétologie (PNP) and the Investments for the Future programme IdEx, Université de Bordeaux/RR1 ORIGINS. This research was carried out in part at the Jet Propulsion Laboratory, California Institute of Technology, under a contract with the National Aeronautics and Space Administration (80NMO018D0004). This work is partly supported by MEXT/JSPS KAKENHI grant numbers JP15H02063, JP18H05439, JP18H05442, JP21K13955, JP21K20376 and JP22000005 and JST CREST grant number JPMJCR1761. This paper is based on observations made with the MuSCAT3 instrument, developed by the Astrobiology Center and under financial supports by JSPS KAKENHI (grant number JP18H05439) and JST PRESTO (grant number JPMJPR1775), at Faulkes Telescope North on Maui, HI, operated by the Las Cumbres Observatory. Observations made with the Wide-Field Camera (WFCam) on the UKIRT telescope were granted through Director's Discretionary Time. UKIRT is owned by the University of Hawaii (UH) and operated by the UH Institute for Astronomy. This research has made use of the NASA Exoplanet Archive, which is operated by the California Institute of Technology, under contract with the National Aeronautics and Space Administration under the

Exoplanet Exploration Program. The Digitized Sky Surveys were produced at the Space Telescope Science Institute under US Government grant number NAG W-2166. The images of these surveys are based on photographic data obtained using the Oschin Schmidt Telescope on Palomar Mountain and the UK Schmidt Telescope. The plates were processed into the present compressed digital form with the permission of these institutions. The National Geographic Society–Palomar Observatory Sky Atlas (POSS-I) was made by the California Institute of Technology with grants from the National Geographic Society. The Second Palomar Observatory Sky Survey (POSS-II) was made by the California Institute of Technology with funds from the National Science Foundation, the National Geographic Society, the Sloan Foundation, the Samuel Oschin Foundation and the Eastman Kodak Corporation. The Oschin Schmidt Telescope is operated by the California Institute of Technology and Palomar Observatory. The UK Schmidt Telescope was operated by the Royal Observatory Edinburgh, with funding from the UK Science and Engineering Research Council (later the UK Particle Physics and Astronomy Research Council) until June 1988, and thereafter by the Anglo-Australian Observatory. The blue plates of the southern Sky Atlas and its Equatorial Extension (together known as the SERC-J), as well as the Equatorial Red (ER) and the Second Epoch [red] Survey (SES), were all taken with the UK Schmidt Telescope. Supplemental funding for sky-survey work at the STScI is provided by the European Southern Observatory.

## Author contributions

M. Gillon initiated the SPECULOOS project, performed the analyses of the photometry described in this paper and wrote a large part of the paper. M. Gillon, B.-O.D., J.d.W., D.Q. and A.H.M.J.T. led the SPECULOOS project and manage its funding, its organization and its operations. P.P.P. developed and maintains the SPECULOOS database and its web interface, a key element in the discovery of the planet. B.V.R. and C.A.T. acquired, reduced and analysed the SpeX spectra, and B.V.R. analysed the TESS data with J.d.W. E.D. managed the scheduling of the SPECULOOS observations. A.Y.B. managed operations of the SPECULOOS-North facility. S.Z.-F. managed the SPECULOOS-South Observatory facilities. M.J.H. managed the SPECULOOS data analysis pipeline. This role was previously in the hands of C.A.M. (who developed the pipeline). M. Gillon, A.H.M.J.T., B.-O.D., G.D., Y.T.D., M.R.S., T.B., M.J.H., S.J.T., C.J.M., E.D., K.B., P.P.P., A.Y.B., L.D., M. Timmermans, F.J.P., S.Z.-F., E.J., L.J.G., C.A.M., D.B., F.D., S.H., Y.S., Z.L.d.B. and P.N. operated the SPECULOOS telescopes. E.D., G.D., L.D., D.S., M. Timmermans, F.J.P. and S.Z.-F. examined the SPECULOOS light curves on a daily basis to search for any structure that could be related to the transit of an exoplanet, and identified the first transits of the planet. L.J.G. contributed to the data management and maintenance of the SPECULOOS different observatories. M.N.G. contributed to the search for SPECULOOS candidates in the TESS data, and provided comments on the paper. M.S. provided comments on the paper. K.G.S. performed the spectral energy distribution analysis. S.M.L. led the UKIRT observation proposal, and managed the scheduling of the UKIRT observations. A.J.B. and R.G. acquired, reduced and analysed the Kast optical spectrum. C.A. led the kinematic and metallicity age analysis. S.B.H. obtained the Gemini high-resolution speckle observations, reduced the data and provided their analysis. S.B.H. also provided comments on the paper. Z.B. managed the Oukaimeden Observatory hosting TRAPPIST-North. M. Ghachoui scheduled and performed the TRAPPIST-North observations. K.B. provided SPECULOOS, Saint-EX, TRAPPIST-North and MuSCAT3 data reduction. N.N. obtained MuSCAT3 Director's Discretionary Time and performed all MuSCAT3 observations. J.P.d.L. reduced data from MuSCAT2 and part of the data from MuSCAT3. N.N., J.P.d.L., A.F., I.F., Y.H., K. Ikuta, K. Isogai, M.I., K.K., T.K., Y.K., J.H.L.,

M.M., M. Tamura, Y.T. and N.W. provided MuSCAT3 GTO for this project. N.N. and E.P. provided MuSCAT2 observations for this project. F.M. performed MuSCAT2 observations. C.A.C. provided the 'Alopeke data reduction. R.A. and R.R. wrote the GTC/HiPERCAM observation proposal, and R.A. reduced the data. F.J.P. searched for extra planets in the TESS data and established detection limits. F.J.P. also scheduled, reduced and analysed the T150 photometric data, and provided the CARMENES data. P.J.A., J.A. and R.V. wrote the CARMENES proposal and managed the schedule of observations and data reduction and analysis. D.S. assessed the potential to measure the planets mass using high-resolution spectroscopy. A.S. operated the T150 telescope. L.D. and E.D. assessed the potential of the planet for emission spectroscopy with JWST and performed the corresponding PandExo simulations. R.H., D.D.B.K. and X.L. provided model emission spectra for various surface compositions. M. Turbet and F.S. performed 3D numerical climate model simulations of SPECULOOS-3 b for two plausible atmospheres, and provided associated emission spectra. E.B. provided guidance and comments on the paper. S.J.T. helped in the design and commissioning of the SPECULOOS-South Observatory and is a member of the operations team. F.S. worked on synthetic observations with JWST. J.J.M. implemented a custom autoguiding routine for each SPECULOOS node based on his open source Donuts science frame autoguiding algorithm, with the goal of minimizing star drift and systematic noise in the observations. M.J.H. mainlined and developed the pipeline that automatically processes all SPECULOOS data at the University of Cambridge and provided an initial fit to the SPECULOOS and TESS transit light curves. V.V.G. ran stellar evolution modelling to derive host star properties. B.-O.D., U.S., Y.G.M.C., D.K., E.A.M.V., I.P.-F., L.S., N.S. and F.Z.L. operated the SAINT-EX telescope, including scheduling observations, nightly operations, data processing and maintenance of the facility. K.H. and M. L. contributed to the funding of SAINT-EX.

## Competing interests

The authors declare no competing interests.

## Additional information

**Extended data** is available for this paper at <https://doi.org/10.1038/s41550-024-02271-2>.

**Supplementary information** The online version contains supplementary material available at <https://doi.org/10.1038/s41550-024-02271-2>.

**Correspondence and requests for materials** should be addressed to Michaël Gillon.

**Peer review information** *Nature Astronomy* thanks the anonymous reviewers for their contribution to the peer review of this work.

**Reprints and permissions information** is available at [www.nature.com/reprints](http://www.nature.com/reprints).

**Publisher's note** Springer Nature remains neutral with regard to jurisdictional claims in published maps and institutional affiliations.

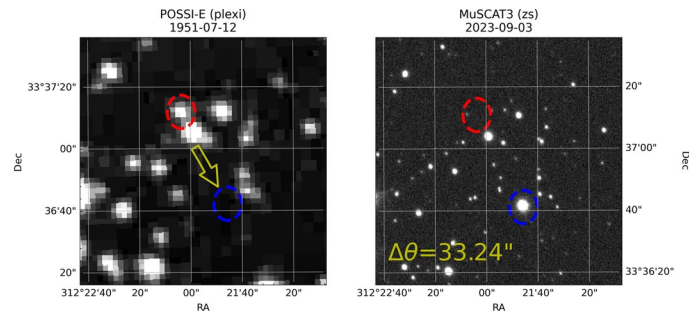
Springer Nature or its licensor (e.g. a society or other partner) holds exclusive rights to this article under a publishing agreement with the author(s) or other rightsholder(s); author self-archiving of the accepted manuscript version of this article is solely governed by the terms of such publishing agreement and applicable law.

© The Author(s), under exclusive licence to Springer Nature Limited 2024

Michaël Gillon <sup>1</sup>✉, Peter P. Pedersen <sup>2,3</sup>, Benjamin V. Rackham <sup>4,5</sup>, Georgina Dransfield<sup>6</sup>, Elsa Ducrot <sup>1,7</sup>,  
 Khalid Barkaoui <sup>1,4,8</sup>, Artem Y. Burdanov <sup>4</sup>, Urs Schrottengger<sup>9</sup>, Yilen Gómez Maqueo Chew <sup>10</sup>, Susan M. Lederer<sup>11</sup>,  
 Roi Alonso <sup>8,12</sup>, Adam J. Burgasser<sup>13</sup>, Steve B. Howell<sup>14</sup>, Norio Narita <sup>8,15,16</sup>, Julien de Wit <sup>4</sup>, Brice-Olivier Demory <sup>9</sup>,  
 Didier Queloz<sup>2,3</sup>, Amaury H. M. J. Triaud <sup>6</sup>, Laetitia Delrez <sup>1,17,18</sup>, Emmanuël Jehin<sup>17</sup>, Matthew J. Hooton <sup>2</sup>,  
 Lionel J. Garcia<sup>1,19</sup>, Clàudia Jano Muñoz<sup>2</sup>, Catriona A. Murray <sup>20</sup>, Francisco J. Pozuelos <sup>21</sup>, Daniel Sebastian <sup>6</sup>,  
 Mathilde Timmermans<sup>1</sup>, Samantha J. Thompson <sup>2</sup>, Sebastián Zúñiga-Fernández <sup>1</sup>, Jesús Aceituno <sup>21,22</sup>,  
 Christian Aganze<sup>13,23</sup>, Pedro J. Amado <sup>21</sup>, Thomas Baycroft <sup>6</sup>, Zouhair Benkhaldoun <sup>24</sup>, David Berardo<sup>3,5,25</sup>,  
 Emeline Bolmont <sup>26,27</sup>, Catherine A. Clark <sup>28,29</sup>, Yasmin T. Davis<sup>6</sup>, Fatemeh Davoudi <sup>1</sup>, Zoë L. de Beurs<sup>4</sup>,  
 Jerome P. de Leon<sup>30</sup>, Masahiro Ikoma <sup>31,32,33</sup>, Kai Ikuta<sup>30</sup>, Keisuke Isogai <sup>30,34</sup>, Izuru Fukuda<sup>30</sup>, Akihiko Fukui <sup>8,15</sup>,  
 Roman Gerasimov<sup>13,35</sup>, Mourad Ghachoui<sup>1,24</sup>, Maximilian N. Günther <sup>36</sup>, Samantha Hasler <sup>4</sup>, Yuya Hayashi<sup>30</sup>,  
 Kevin Heng<sup>37</sup>, Renyu Hu <sup>28,38</sup>, Taiki Kagetani<sup>30</sup>, Yugo Kawai <sup>30</sup>, Kiyoe Kawauchi<sup>39</sup>, Daniel Kitzmann <sup>9</sup>,  
 Daniel D. B. Koll <sup>40</sup>, Monika Lendl <sup>26</sup>, John H. Livingston <sup>16,32,41</sup>, Xintong Lyu <sup>40</sup>, Erik A. Meier Valdés <sup>9</sup>,  
 Mayuko Mori <sup>30</sup>, James J. McCormac<sup>42</sup>, Felipe Murgas <sup>8,11</sup>, Prajwal Niraula<sup>4</sup>, Enric Pallé <sup>7,12</sup>, Ilse Plauchu-Frayn<sup>43</sup>,  
 Rafael Rebolo <sup>8</sup>, Laurence Sabin <sup>43</sup>, Yannick Schackey<sup>3</sup>, Nicole Schanche<sup>44,45</sup>, Franck Selsis <sup>46</sup>, Alfredo Sota <sup>21</sup>,  
 Manu Stalport<sup>1,17</sup>, Matthew R. Standing<sup>6,47</sup>, Keivan G. Stassun <sup>48</sup>, Motohide Tamura <sup>16,41,49</sup>, Yuka Terada<sup>42,43</sup>,  
 Christopher A. Theissen <sup>13</sup>, Martin Turbet <sup>46,50</sup>, Valérie Van Grootel <sup>17</sup>, Roberto Varas <sup>21</sup>, Noriharu Watanabe<sup>30</sup>  
 & Francis Zong Lang<sup>9</sup>

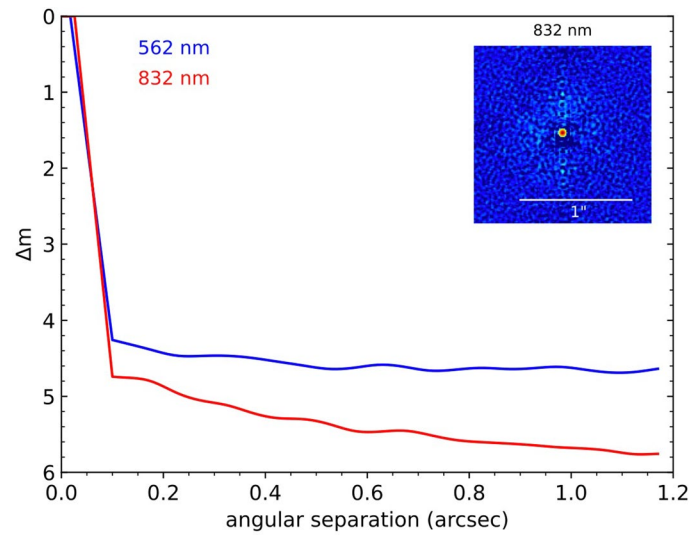
<sup>1</sup>Astrobiology Research Unit, Université de Liège, Liège, Belgium. <sup>2</sup>Cavendish Laboratory, Cambridge, UK. <sup>3</sup>Department of Physics, ETH Zurich, Zurich, Switzerland. <sup>4</sup>Department of Earth, Atmospheric and Planetary Science, Massachusetts Institute of Technology, Cambridge, MA, USA. <sup>5</sup>Kavli Institute for Astrophysics and Space Research, Massachusetts Institute of Technology, Cambridge, MA, USA. <sup>6</sup>School of Physics & Astronomy, University of Birmingham, Birmingham, UK. <sup>7</sup>LESIA, Observatoire de Paris, CNRS, Université Paris Diderot, Université Pierre et Marie Curie, Meudon, France. <sup>8</sup>Instituto de Astrofísica de Canarias (IAC), La Laguna, Spain. <sup>9</sup>Center for Space and Habitability, University of Bern, Bern, Switzerland. <sup>10</sup>Instituto de Astronomía, Universidad Nacional Autónoma de México, Mexico City, Mexico. <sup>11</sup>NASA Johnson Space Center, Houston, TX, USA. <sup>12</sup>Departamento de Astrofísica, Universidad de La Laguna, La Laguna, Spain. <sup>13</sup>Department of Astronomy & Astrophysics, University of California San Diego, La Jolla, CA, USA. <sup>14</sup>NASA Ames Research Center, Moffett Field, CA, USA. <sup>15</sup>Komaba Institute for Science, The University of Tokyo, Tokyo, Japan. <sup>16</sup>Astrobiology Center, Tokyo, Japan. <sup>17</sup>Space Sciences, Technologies and Astrophysics Research (STAR) Institute, Université de Liège, Liège, Belgium. <sup>18</sup>Institute of Astronomy, KU Leuven, Leuven, Belgium. <sup>19</sup>Center for Computational Astrophysics, Flatiron Institute, New York, NY, USA. <sup>20</sup>Department of Astrophysical and Planetary Sciences, University of Colorado Boulder, Boulder, CO, USA. <sup>21</sup>Instituto de Astrofísica de Andalucía (IAA-CSIC), Granada, Spain. <sup>22</sup>Centro Astronómico Hispano en Andalucía, Gérgal, Spain. <sup>23</sup>Department of Physics, Stanford University, Stanford, CA, USA. <sup>24</sup>Oukaimeden Observatory, High Energy Physics and Astrophysics Laboratory, Faculty of Sciences Semlalia, Cadi Ayyad University, Marrakech, Morocco. <sup>25</sup>Department of Physics, Massachusetts Institute of Technology, Cambridge, MA, USA. <sup>26</sup>Département d'astronomie de l'Université de Genève, Sauverny, Switzerland. <sup>27</sup>Centre sur la Vie dans l'Univers, Université de Genève, Geneva, Switzerland. <sup>28</sup>Jet Propulsion Laboratory, California Institute of Technology, Pasadena, CA, USA. <sup>29</sup>NASA Exoplanet Science Institute, IPAC, California Institute of Technology, Pasadena, CA, USA. <sup>30</sup>Department of Multi-Disciplinary Sciences, Graduate School of Arts and Sciences, The University of Tokyo, Tokyo, Japan. <sup>31</sup>Division of Science, National Astronomical Observatory of Japan, Tokyo, Japan. <sup>32</sup>Astronomical Science Program, Graduate University for Advanced Studies, Tokyo, Japan. <sup>33</sup>Department of Earth and Planetary Science, The University of Tokyo, Tokyo, Japan. <sup>34</sup>Okayama Observatory, Kyoto University, Asakuchi, Japan. <sup>35</sup>Department of Physics & Astronomy, University of Notre Dame, Notre Dame, IN, USA. <sup>36</sup>European Space Research and Technology Centre (ESTEC), European Space Agency (ESA), Noordwijk, the Netherlands. <sup>37</sup>Faculty of Physics, Ludwig Maximilian University, Munich, Germany. <sup>38</sup>Division of Geological and Planetary Sciences, California Institute of Technology, Pasadena, CA, USA. <sup>39</sup>Department of Physical Sciences, Ritsumeikan University, Kusatsu, Japan. <sup>40</sup>Department of Atmospheric and Oceanic Sciences, Peking University, Beijing, China. <sup>41</sup>National Astronomical Observatory of Japan, Tokyo, Japan. <sup>42</sup>Department of Physics, University of Warwick, Coventry, UK. <sup>43</sup>Instituto de Astronomía, Universidad Nacional Autónoma de México, Unidad Académica en Ensenada, Ensenada, Mexico. <sup>44</sup>NASA Goddard Space Flight Center, Greenbelt, MD, USA. <sup>45</sup>Department of Astronomy, University of Maryland, College Park, MD, USA. <sup>46</sup>Laboratoire d'astrophysique de Bordeaux, Université Bordeaux, CNRS, Pessac, France. <sup>47</sup>European Space Astronomy Centre (ESAC), European Space Agency (ESA), Madrid, Spain. <sup>48</sup>Department of Physics and Astronomy, Vanderbilt University, Nashville, TN, USA. <sup>49</sup>Department of Astronomy, University of Tokyo, Tokyo, Japan. <sup>50</sup>Laboratoire de Météorologie Dynamique/IPSL, CNRS, Sorbonne Université, Ecole Normale Supérieure, Université PSL, Ecole Polytechnique, Institut Polytechnique de Paris, Paris, France.

✉e-mail: [michael.gillon@uliege.be](mailto:michael.gillon@uliege.be)



**Extended Data Fig. 1 | Evolution of the position of SPECULOOS-3.** Left: Archival image of the target taken in 1951 using a photographic plate on the Palomar Schmidt Telescope as part of the National Geographic Society - Palomar Observatory Sky Atlas (POSS-I) survey. Right: MuSCAT3<sub>z</sub> band image taken in

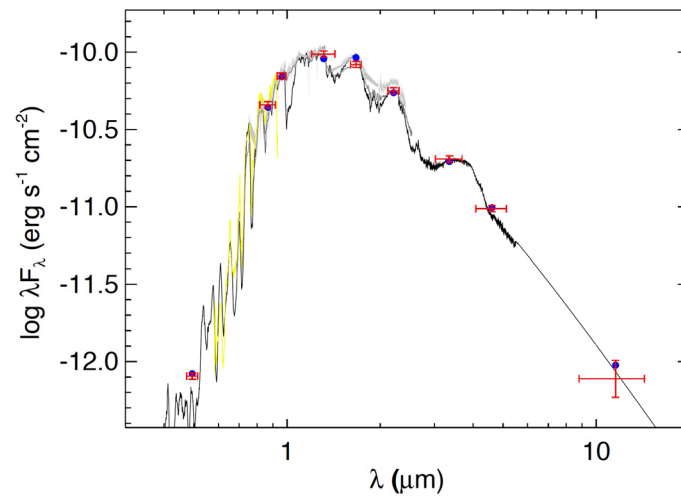
2023. The 7 decade-long baseline allowed the target move more than half a degree showing a clear line-of-sight at the past (red circle) and current (blue circle) positions of the target.



**Extended Data Fig. 2 | Speckle imaging of SPECULOOS-3.** Result from speckle imaging with the Alopeke instrument mounted on the 8-m Gemini-North telescope, on Mauna Kea, Hawai'i. The inset on the top right shows the final image produced by our analysis, which is summarized by the two curves of the

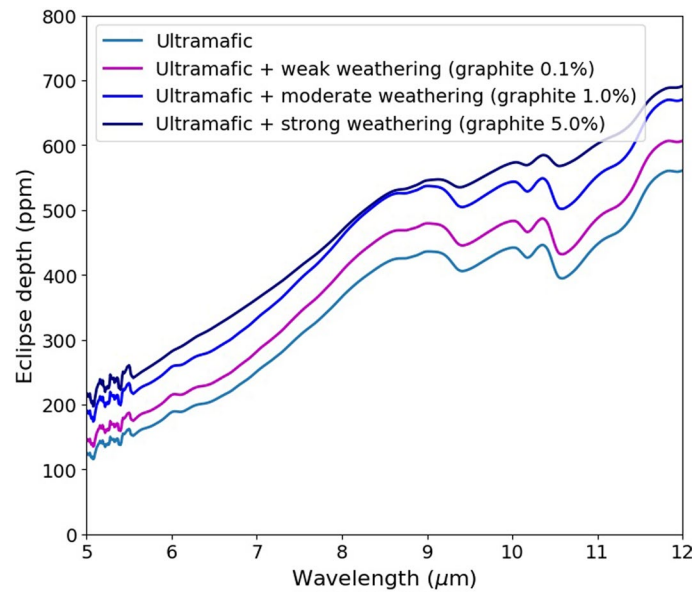
main figure. These curves show the sensitivity in two bands (blue = 562 nm and red = 832 nm). The observations reveal there are no companions with a brightness greater than 5 to 6 magnitudes at distances above 0.1" from SPECULOOS-3A, which corresponds to a physical distance of approximately 1.7 AU.





**Extended Data Fig. 3 | Spectral energy distribution of SPECULOOS-3.** Red symbols represent the observed photometric measurements, where the horizontal bars represent the effective width of the bandpass, and the vertical bars the 1- $\sigma$  error bars on the measurements. Blue symbols are the model

fluxes from the best-fit PHOENIX atmosphere model (black). Overlaid on the model are the absolute flux-calibrated spectrophotometric observations from SpeX (gray swathe) and Kast (yellow).



**Extended Data Fig. 4 | Effect of space weathering on the emission spectrum of an airless SPECULOOS-3b.** Mid-infrared eclipse depths increase with stronger weathering of an ultramafic surface (see Methods for details).

**Extended Data Table 1 | Detectability of atmospheres with MIRI/LRS**

	10 bar CO <sub>2</sub>	10 bar H <sub>2</sub> O
Blackbody	<b>4</b>	<b>4</b>
Basaltic	<b>7</b>	<b>6</b>
10 bar CO <sub>2</sub>	–	<b>9</b>
10 bar H <sub>2</sub> O	<b>9</b>	–

Number of occultation observations with MIRI/LRS needed to distinguish the CO<sub>2</sub> and H<sub>2</sub>O atmospheric models from two common airless planet models. These numbers were obtained using wavelength bins of constant resolution  $R=3$ .

**Extended Data Table 2 | Detectability of surface mineralogy with MIRI/LRS**

	Blackbody	Metal-rich	Ultramafic	Feldspathic	Basaltic	Granitoid	Fe-oxidized
Blackbody	–	≥30	6	3	17	3	21
Metal-rich	≥30	–	9	4	≥30	3	≥30
Ultramafic	10	15	–	10	20	7	18
Feldspathic	4	5	14	–	6	≥30	5
Basaltic	≥30	≥30	16	5	–	4	≥30
Granitoid	3	5	9	≥30	5	–	4
Fe-oxidized	≥30	≥30	12	5	≥30	4	–

Number of secondary eclipse observations needed with MIRI/LRS to characterize the surface of SPECULOOS-3 b. The distinguishability of models was not analysed beyond 30 eclipses. Ten eclipse observations should allow to distinguish 50% of competing surface models with 4  $\sigma$  confidence (and 70% at 2  $\sigma$ ).